Tectonophysics 879 (2024) 230322

Contents lists available at ScienceDirect

Tectonophysics

journal homepage: www.elsevier.com/locate/tecto

Magnitudes and surface rupture lengths of paleo-earthquakes at the NW-part of the Peel Boundary fault zone, Roer Valley Rift System

R.T. Van Balen [a,b,*], R.E. Lapperre [a], H.A.G. Woolderink [a,c], J. Wallinga [d], C. Kasse [a]

[a] Department of Earth Sciences, VU University Amsterdam, De Boelelaan 1085, Amsterdam 1081 HV, the Netherlands
[b] TNO - Geological Survey of the Netherlands, Princetonlaan 6, Utrecht 3584 CB, the Netherlands
[c] Wageningen Environmental Research, Droevendaalsesteeg, Wageningen 36708 PB, the Netherlands
[d] Netherlands Centre for Luminescence Dating & Soil Geography and Landscape group, Wageningen University & Research, Droevendaalsesteeg 3, Wageningen 6708 PB, the Netherlands

ARTICLE INFO

Keywords:
Paleoseismoloy
North Sea basin
Seismic hazard
Glacio-isostasy
Lower Rhine Graben

ABSTRACT

The Peel Boundary Fault zone (PBFZ) is the 125 km long, seismically active, northern bounding fault zone of the Roer Valley Rift System (RVRS). The last damaging earthquake along the PBFZ was the Roermond earthquake of 1992. It had a magnitude of Mw 5.3 and no surface rupture. Previous results from two trenching studies located in the central and southeastern parts of the PBFZ provided evidence for two surface rupturing paleo-earthquakes. The largest earthquake had an estimated magnitude of Mw ~6.8 and a surface rupture length of at least 35 km. As it took place around the Late Pleniglacial – Late Glacial transition a link to glacio-isostatic motions is likely. Results from a new trench situated at the northwestern part of the PBFZ shows evidence for three to four paleo-earthquakes, of which three were surface rupturing. These comprise two normal faulting- and one, younger trans-tensional displacement. The normal faulting events have ~1 m vertical displacements each, which translate into magnitudes of Mw ~7. Like the previous results, they occurred during the Late Pleniglacial-Late Glacial transition, at ~15 ka and ~ 14 ka. The younger trans-tensional event occurred sometime during the Holocene, pre-dating an unaffected, 13th century man-made paleo-channel on the hangingwall. The potential fourth, non-surface rupturing earthquake is indirectly evidenced by loading deformations of a sand layer and a collapsed brick-wall in the infill of the paleo-channel. Comparison of our trenching results to those from the two previous studies, which were located farther to the southeast along the PBFZ, shows that for one event a correlation is possible. The correlation would indicate a surface rupture length of at least 55 km. Combined, all trenching results indicate that the characteristic maximum rupturing displacement is ~1 m, and thus that Mw ~7 is the maximum magnitude of paleo-earthquakes along the PBFZ.

1. Introduction

The Roer Valley Rift System (RVRS) is located in the southern part of the Netherlands and adjoining areas in Belgium and Germany (Fig. 1; Geluk et al., 1994). The last rifting phase of the RVRS started during the Late Oligocene-Miocene transition and is still ongoing (Geluk et al., 1994; Michon et al., 2003; Van Balen et al., 2005) as, for example, evidenced by earthquakes (e.g. Camelbeeck et al., 2007; Hinzen et al., 2021). The last damaging earthquake in the RVRS was the Roermond earthquake of 1992 (Ml 5.8; Mw 5.3) which took place along the Peel Boundary Fault zone (PBFZ) (Fig. 2; Van Eck and Davenport, 1994). Surface ruptures have not taken place during historical times, which is likely due to the long recurrence interval of large earthquakes in the RVRS (Camelbeeck et al., 2007; Vanneste et al., 2013) or, alternatively, due to the diminishing glacio-isostatic driving mechanism (see below; Van Balen et al., 2019, 2021).

Pronounced fault scarps, fluvial tectonic geomorphology and results from trench studies provide ample evidence for larger, surface rupturing earthquakes in pre-historic times (e.g. Camelbeeck et al., 2007; Grützner et al., 2016; Van Balen et al., 2019, 2021; Vanneste et al., 2018; Woolderink et al., 2018, 2019). Results from two previous trench studies at the PBFZ, located at the central and southeastern parts (Fig. 2), showed that the last large, surface rupturing event occurred during the Late Pleniglacial - Late Glacial transition. It had a maximum vertical displacement of ~1 m and a rupture length of at least 32 km (the distance between the two trenches; Van Balen et al., 2019). However, the

* Corresponding author at: Department of Earth Sciences, VU University Amsterdam, De Boelelaan 1085, Amsterdam 1081 HV, the Netherlands.
E-mail address: r.t.van.balen@vu.nl (R.T. Van Balen).

https://doi.org/10.1016/j.tecto.2024.230322
Received 2 February 2024; Received in revised form 16 April 2024; Accepted 20 April 2024
Available online 22 April 2024

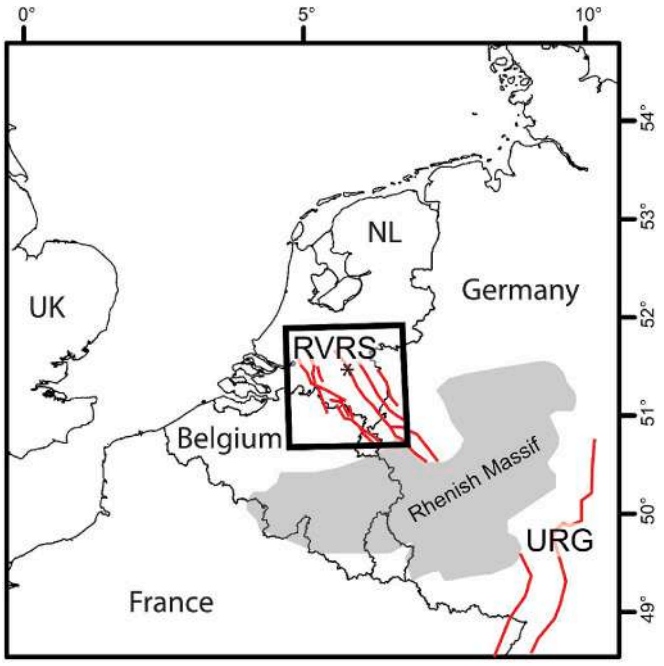

Fig. 1. Location of the study area in Northwestern Europe. RVRS = Roer Valley Rift System, URG = Upper Rhine Graben, NL = the Netherlands, UK = United Kingdom. Red lines represent major fault zones. The rectangle shows the position of Fig. 2. Coordinate system is in lat-lon using UTM projection. The asterisk indicates the approximate location of the trench near Uden. (For interpretation of the references to colour in this figure legend, the reader is referred to the web version of this article.)

PBFZ has a length of at least 125 km, from the southeast, just across the border in Germany (Woolderink et al., 2019) to the northwest, where faults of the PBFZ are buried by deposits of the Holocene Rhine-Meuse delta (Cohen et al., 2002, 2005; Vanneste et al., 2013). Thus, rupture lengths and -offsets may have been larger, and, consequently, the maximum magnitude of paleo- earthquakes can have exceeded Mw ~6.8, as derived from the already available evidence provided by the previous trenches. Alternatively, the PBFZ may consists of rupturing segments with different earthquake histories. Vanneste et al. (2013), for example, consider ~55 km as the longest credible rupture length in the RVRS, implying at least 2 rupturing segments.

The most pronounced and highest fault scarps of the PBFZ are located in its northwestern part, near Uden (Figs. 2, 3; Michon and Van Balen, 2005; Van Balen et al., 2005). The topographic offset at these scarps is 3–5 m, compared to 1–1.5 m scarp height at the previously trenched sites (Fig. 2; Michon and Van Balen, 2005). The larger height suggests larger and/or more frequent paleo-earthquakes. In addition, the scarps near Uden are adjacent to the maximum depth of the base Miocene deposits in the RVRS (Fig. 2; Michon et al., 2003), implying that the largest total Neogene fault displacement occurs here, and not at the two previously trenched sites. However, no information on the paleoseismic history of this part of the fault zone is available yet. The current study, therefore, focusses on the northwestern part of the PBFZ, and has the following objectives: 1) to determine the earthquake history in this part of the PBFZ, and 2) to further constrain rupture lengths by correlating the results to the previous trenches.

2. Setting

2.1. Tectonic setting

The Roer Valley Rift System (RVRS) is situated in the northwestern part of the European Cenozoic Rift System (ECRIS; Ziegler, 1992; Michon et al., 2003). The origin of the RVRS dates back to the early Carboniferous, when extension affected Avalonia (Smit et al., 2018). Faults of the RVRS have been repeatedly reactivated in normal and reverse faulting modes during the Mesozoic and Cenozoic (Geluk et al., 1994) evidencing long lived lithosphere memory. The last extension phase of the RVRS started during the Late Oligocene (Ziegler, 1992; Michon et al., 2003) and is still ongoing (Houtgast and Van Balen, 2000; Michon and Van Balen, 2005; Van Balen et al., 2005) as for example evidenced by occasional earthquakes (e.g. Camelbeeck et al., 2007; Hinzen et al., 2021). This last extension phase is the effect of Alpine compression on its foreland (Ziegler, 1992). Since the Middle Pleistocene the southeastern part of the RVRS also experiences uplift as a result of a mantle plume centered beneath the volcanic Eifel area (e.g. Van Balen et al., 2000; Demoulin and Hallot, 2009). As shown by Gold et al. (2017), this uplift caused an increase of fault displacement rates in the southeastern part of the RVRS. Most earthquakes in the past 25 years occurred within an area corresponding to maximum crustal dilatation caused by this still ongoing plume-induced uplift (Kreemer et al., 2020; Hinzen et al., 2021).

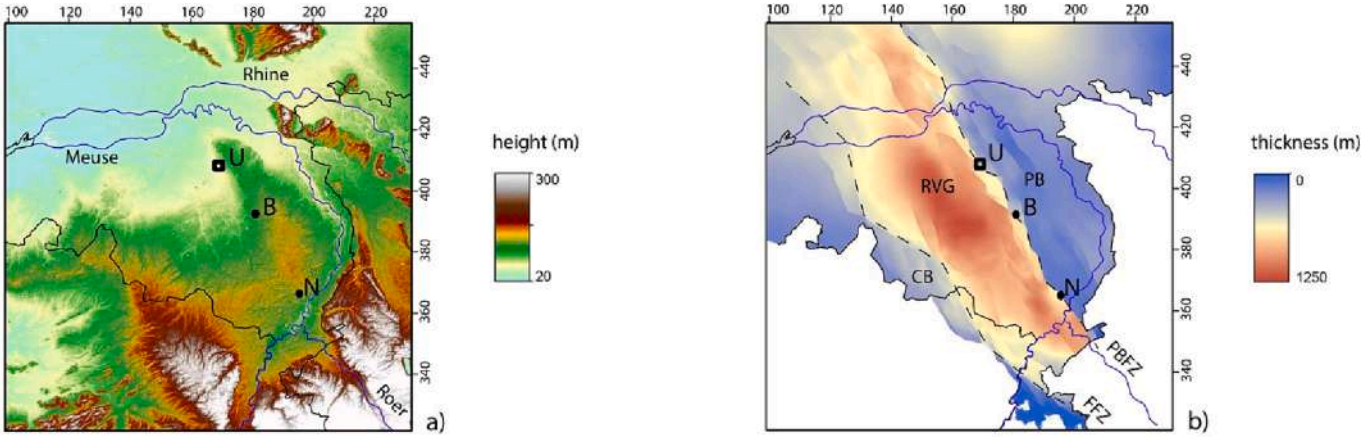

Fig. 2. Location and overview figures. Coordinate system is the Dutch National Grid (RD); axis units are in km's.
a) Digital elevation model showing the topography of the Roer Valley Rift System and location of the study area. The 'N' denotes the location of the previous Neer trench (Van den Berg et al., 2002), and 'B' the Bakel trench (Van Balen et al., 2019). Branches of the Rhine-Meuse fluvial system cross the faults of the RVRS. Further to the northwest lie the deposits of the Holocene Rhine-Meuse delta. The position of a) is indicated in Fig. 1.
b) Depth to the base of the Miocene deposits, reflecting the differential neotectonic vertical motions in the rift system (data not available outside the Netherlands). PBFZ = Peel Boundary Fault Zone, FFZ = Feldbiss Fault Zone, RVG = Roer Valley Graben, CB = Campine Block, PB = Peel Block.

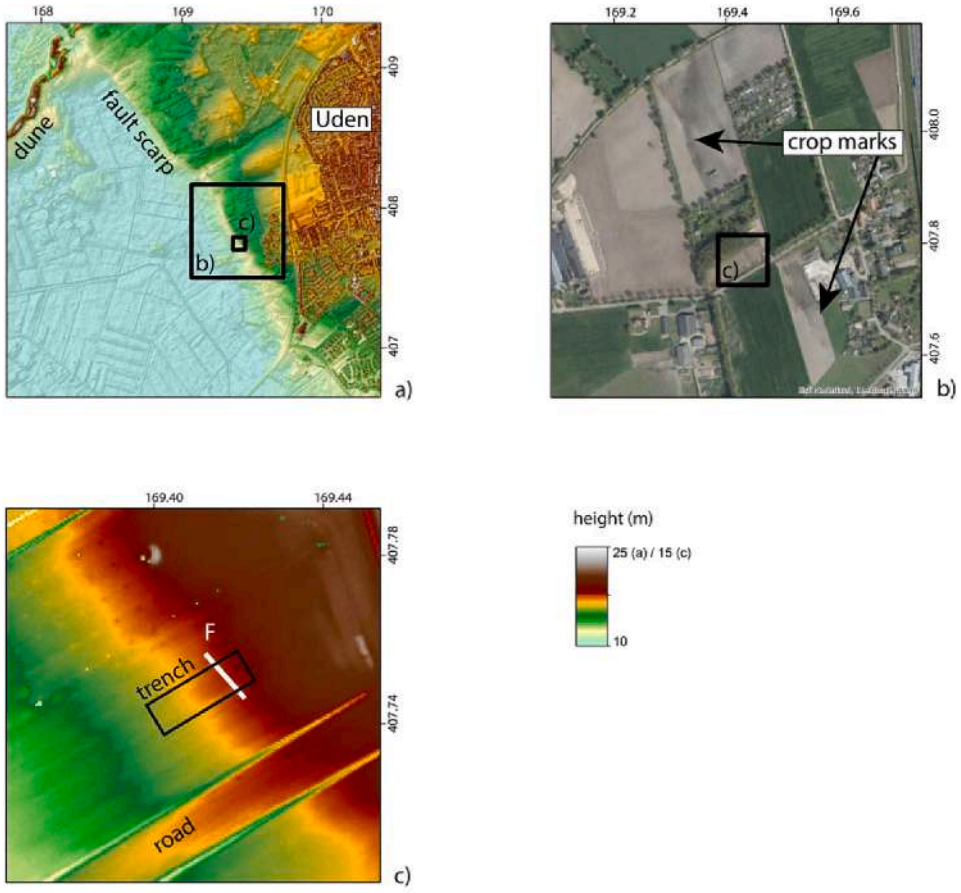

Fig. 3. Detailed maps. Coordinate system is the Dutch National Grid (RD); axis units are in km's.
a) Digital elevation map of the fault scarp near Uden; maximum height is 25 m. The location is depicted by a rectangle in Figs. 2a, b.
b) Aerial photograph of the area corresponding to the outer rectangle on a). The fault trace is marked by crop- and soil marks.
c) Detailed digital elevation model of the area surrounding the trench site. The position is indicated on a) and b); the maximum height is 15 m. The location of the fault (F) is indicated with a white line.

The Feldbiss Fault zone (FFZ) and the Peel Boundary Fault zone (PBFZ), the southern- respectively northern bounding fault zones of the RVRS, are the seismically most active fault zones (Camelbeeck et al., 2007; Vanneste et al., 2018). The earthquake history of the PBFZ has previously been studied in two trenches. In the Bakel trench, located in the central part of the PBFZ (Fig. 2), the oldest surface rupturing event occurred during the Older Dryas (~14 ka; Mw 6.8 ± 0.3, estimated based on ~1 m fault offset), followed by a smaller event directly after the Allerød (0.2–0.1 m; 13.9–12.9 ka; Van Balen et al., 2019). Events with a similar (but less precise) age and smaller offset, were reconstructed in the Neer trench in the southeastern part of the PBFZ (oldest event 0.55 m offset; last displacement 0.30 m; Van den Berg et al., 2002).

The inferred ~Mw 6.8 ± 0.3 magnitude is in agreement with the maximum earthquake size based on the 25 km thickness of the seismogenic layer of the RVRS (Wells and Coppersmith, 1994; Hinzen et al., 2021), with the inferred maximum magnitude based on the logarithmic frequency-magnitude relationship for the RVRS area (Camelbeeck et al., 2007) and with trenching-based results along the FFZ (Vandenberghe et al., 2009; Vanneste et al., 2018; Van Balen et al., 2021). Although also older and younger (including Holocene) surface rupturing events have been inferred in trench studies in the RVRS (e.g. Camelbeeck et al., 2007; Vandenberghe et al., 2009; Grützner et al., 2016), the timing of by far most of the surface rupturing earthquakes suggests a relation with the Weichselian deglaciation of NW Europe (Houtgast et al., 2005). A plausible triggering mechanism is the collapse of the glacio-isostatic forebulge (e.g. Houtgast et al., 2005; Van Balen et al., 2019, 2021). The same triggering mechanism has been proposed for paleoearthquakes along the FFZ (Houtgast et al., 2005; Van Balen et al., 2021), and for seismic activity of faults and fault zones in northwestern Europe located closer to the former glacial margin (Mörner, 1978, 2013; Brandes et al., 2012, 2015, 2018; Sandersen and Jørgensen, 2014; Steffen et al., 2014; Müller et al., 2020). Modelling of the effect of surface loading over a glacial cycle confirm that glacio-isostatic adjustments can trigger faulting in the RVRS (Steffen et al., 2014; Craig et al., 2023; Damon et al., 2023). Dating results on volcanic eruptions related to the plume below the Eifel indicate that also they are likely triggered by glacio-isostatic motions (Nowell et al., 2006). The youngest series of eruptions started at around 15.5 ± 1.1 ka ago, the last event occurred 10.940 ± 90 cal BP (note, the famous Laacher See Volcano eruption dates at 12.960 ± 140 cal BP; Schmidt et al., 2017).

2.2. Stratigraphy

In the wider study area the shallow deposits consist of coarse-grained sediments deposited by the Meuse river (Beegden Formation), overlain by fine-grained sand and loam deposits, formed in local fluvial, aeolian and lacustrine environments (Boxtel Formation; Schokker and Koster, 2004; Schokker et al., 2007). The uppermost, aeolian part of the Boxtel Formation corresponds to the classic Weichselian coversand series (e.g. Kasse et al., 2007; Vandenberghe et al., 2013), which occur widespread in large parts of NW and Central Europe.

The general stratigraphy of the current site is similar to the previously studied Bakel trench site, located at a distance of ~25 km, see Van Balen et al. (2019). In summary, in that trench, the stratigraphy

consisted of four units, A-D. Unit A consisted of whitish coarse sand beds with isolated gravel pockets, thin gravel beds and grayish loam layers, representing the Beegden Formation. They have a luminescence age of 286 ± 25 to 262 ± 24 ka . The overlying Unit B consisted of alternating layers of gray sandy loam and yellowish fine sand, containing humic and peat intervals. The unit was heavily deformed by meter-scale involutions, which were interpreted as cryoturbations. ^{14}C dating combined with lithologic characteristics (silt and peat) indicated that this unit represents the Lower Loamy Bed of the coversand series, which was deposited during the Bølling (~14.7–14.0 ka; Kasse et al., 2018). Unit B is overlain by a colluvial wedge Unit C, which consisted of fine and coarse gravelly sands, intercalated with thin gravel beds. On the hanging wall the unit was wedge-shaped, with a thickness of ~1 m at the fault contact and tapering to a thickness of one thin gravel bed away from it. The colluvial wedge is one of the important evidences for surface rupturing. On the footwall the unit had a thickness of one thin gravel bed. Its OSL age is around 14 ka. The uppermost Unit D consists of horizontally bedded, well-sorted sand. The sediments of this unit correspond to the dry aeolian sand sheet deposits of the Younger Coversands I and II (Kasse et al., 2007; 'Facies A' by Schokker and Koster, 2004). On the hangingwall a ~ 15 cm thick, gray, sandy loam layer was present in Unit D. This layer is characterized by charcoal particles and burrowing. The overall characteristics and age of this gray sandy loam showed strong similarities to the Usselo soil, which developed during the Allerød (13.91–12.85 ka Hoek, 2001; Van Hoesel et al., 2012; Vandenberghe et al., 2013; Bazelmans et al., 2021). The OSL dating constraints were in agreement with this age range (see Van Balen et al., 2019) .

3. Methods

3.1. Trench

The location of the new trench site near Uden (northwestern PBFZ) was selected based on information from fault scarps (Michon and Van Balen, 2005), crop- and soil marks (Fig. 3; e.g. Van Balen et al., 2019, 2021; Lapperre et al., 2019) and drillings. The trench was positioned perpendicular to the inferred NW-SE oriented strike of the fault. At the surface, the trench had a length of 25 m and a width of 8 m (Fig. 4). The ~2.5 m depth was just above the artificially lowered groundwater level. At the floor level the trench was 14 m long and 1.8 m wide. The trench walls were approximately 45 degrees inclined. Suction-drillings and temporary pits were used to investigate the stratigraphy below the trench floor. The trench walls were documented with abundant photographs, which have been used to make a 3D model using photogrammetry. Lacquer peel profiles were made after studying the trench walls stratigraphy and structures. A very large composite lacquer peel of the fault zone was used to study the small-scale faulting. A detailed archeological study on the infill of a man-made channel was carried-out on a small section of the southeastern trench wall (Hiddink, 2019).

3.2. Luminescence dating

Twenty samples for luminescence dating were taken from the southeastern trench wall by hammering PVC tubes horizontally into the exposure (Table 1). Samples HB1–8 (NCL-71118081-088) were taken from the footwall, while samples LB9–20 (NCL-71118089-100) were obtained from the hangingwall (Fig. 5). After sampling, the sealed sample tubes were transported to the darkroom facilities of the Netherlands Centre for Luminescence dating, where they were split in two parts. The (light-exposed) material from the outer ends of the tubes was prepared for dose-rate estimation using gamma-spectrometry, through drying, ashing, grinding and mixing with wax to create a Rn-retaining puck. Activity concentrations were converted to infinite matrix dose rates (Guerin et al., 2011), and from these total environmental dose rates were obtained taking into account cosmic radiation, grain-size attenuation and attenuation by moisture and organics. For cosmic radiation (Prescott and Hutton, 1994) we assumed immediate burial to present depth for all samples apart from those obtained from Unit I (gradual burial). Organic contents were determined by weighting samples before and after ashing. Average burial time water content was based on the lithology: 20 ± 3% by weight for sandy fluvial deposits, 20 ± 5% by weight for sandy aeolian deposits and a higher estimate of 30 ± 6% by weight for silty and loamy deposits to account for their higher water holding capacity. For the K-rich feldspar fraction we included the internal dose rate from potassium. Following Smedley et al. (2012) we assume a K-content of 10 ± 2% for the single grain measurements and 12.5 ± 0.5% for single-aliquot measurements (Huntley and Baril, 1997).

Palaeodoses were mainly obtained using quartz optically stimulated luminescence (OSL) dating, while additional post-infrared infrared stimulated (pIRIR) measurements on K-feldspar fractions were performed for samples HB5–7. The quartz grainsize fraction 212–250 μm was purified by sieving and chemical treatment with HCl, H_2O_2, 40% HF and rinsing with 30% HCl. To obtain a K-rich feldspar fraction on the

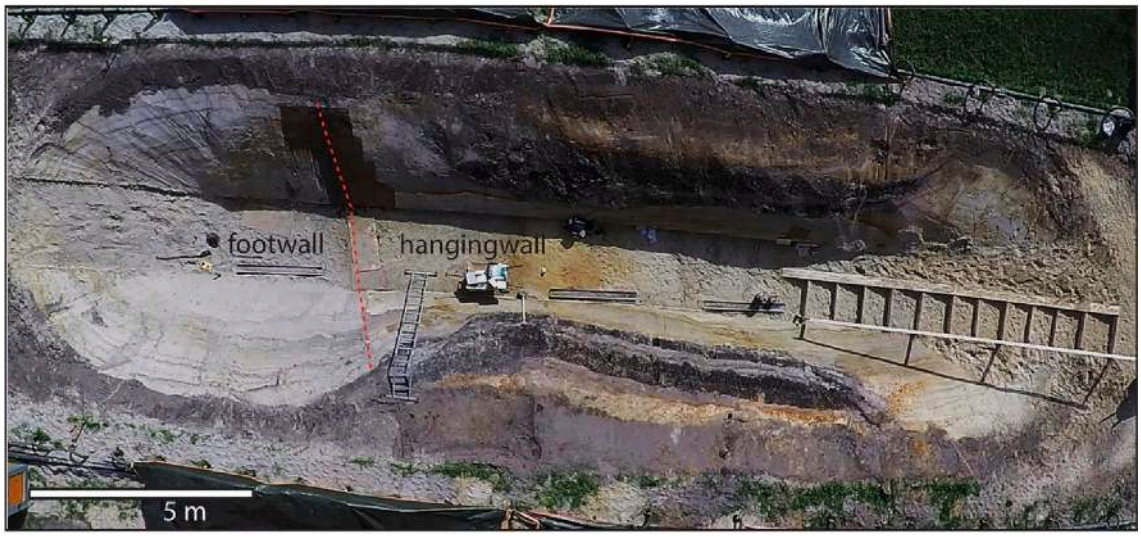

Fig. 4. Overview photo of the trench. The red dashed line indicates the fault. The prominent dark gray to black deposits on the hangingwall are the organic infill of the man-made paleo-channel. The length of the trench is about 25 m and the width 8 m. (For interpretation of the references to colour in this figure legend, the reader is referred to the web version of this article.)

Table 1
Summary of luminescence dating results based on quartz single aliquot OSL dating apart from sample codes with $_{f,SG}$ and $_{f,SA}$ which denote paleodose estimation on feldspar pIRIR using single grain and single-aliquot approaches, respectively. Paleodoses obtained from mean equivalent dose after iterative removal of outliers unless stated otherwise in comments: BS MAM indicates that bootstrapped minimum age model (Galbraith et al., 1999; Cunningham and Wallinga, 2012) was used for paleodose estimation. Overdispersion is determined using the CAM model (Galbraith et al., 1999).

Sample	NCL code 71,118	Depth (m)	Paleodose (Gy)	Dose rate (Gy/ka)	Age (ka)	Reliability	Comments	unit
HB1	081	0.50	13.4 ± 0.4	0.89 ± 0.04	15.0 ± 0.8	OK	Overdispersion 13%	III
HB2	082	0.86	13.0 ± 0.4	0.89 ± 0.04	15.0 ± 0.8	OK	Overdispersion15%	III
HB3	083	1.20	12.4 ± 0.4	0.89 ± 0.04	14.9 ± 0.8	OK	Overdispersion12%	III
HB4	084	1.45	14.9 ± 0.5	1.02 ± 0.03	14.5 ± 0.7	OK	Overdispersion13%	II
HB5	085	1.80	25.7 ± 0.8	1.15 ± 0.04	22.6 ± 1.0	OK	Overdispersion11%	II
HB5	$085_{f,SG}$		38.2 ± 0.8	1.92 ± 0.15	19.9 ± 1.6	Likely OK	Overdispersion19%	
HB6	086	2.25	36.4 ± 0.8	0.81 ± 0.03	45.1 ± 5.2	Questionable	Overdispersion 73%, BS MAM	II
HB6	$086_{f,SA}$		335 ± 59	1.76 ± 0.10	191 ± 35	Questionable	Overdispersion ***	
HB6	$086_{f,SG}$		403 ± 1.8	1.59 ± 0.15	25.3 ± 2.6	Likely OK	Overdispersion 73%, BS MAM	
HB7	087	3.13	241.4 ± 33.6	0.83 ± 0.03	291 ± 42	Doubtful	Overdispersion 21%	I
HB7	$87_{f,SA}$		428 ± 26	1.78 ± 0.10	240 ± 20	Likely OK	Overdispersion	I
HB7	$87_{f,SG}$		353 ± 15	1.62 ± 0.15	218 ± 22	Questionable	Overdispersion56%	I
HB8	088	1.37	123 ± 0.3	0.88 ± 0.04	14.7 ± 0.7	OK	Overdispersion18%	III
LB9	089	0.73	14.6 ± 0.5	1.14 ± 0.05	12.9 ± 0.7	OK	Overdispersion16%	IV
LB10	090	1.31	11.9 ± 0.4	0.90 ± 0.04	13.2 ± 0.7	OK	Overdispersion13%	IV
LB11	091	1.82	12.1 ± 0.5	0.80 ± 0.03	15.2 ± 0.9	OK	Overdispersion13%	III
LB12	092	2.33	12.9 ± 0.5	0.87 ± 0.04	14.8 ± 0.9	OK	Overdispersion16%	III
LB13	093	2.63	19.0 ± 0.9	1.12 ± 0.04	17.0 ± 1.0	Questionable	Overdispersion28%	III
LB14	094	0.66	15.3 ± 0.6	1.28 ± 0.05	11.9 ± 0.7	OK	Overdispersion13%	IV
LB15	095	0.89	12.5 ± 0.4	1.02 ± 0.04	12.3 ± 0.6	OK	Overdispersion11%	IV
LB16	096	1.14	11.3 ± 0.4	0.86 ± 0.04	13.1 ± 0.7	OK	Overdispersion14%	IV
LB17	097	1.20	12.7 ± 0.3	0.94 ± 0.04	13.5 ± 0.7	OK	Overdispersion21%, due to 1 outlier	IV
LB18	098	1.68	12.9 ± 0.5	0.91 ± 0.04	14.2 ± 0.8	OK	Overdispersion23%, due to 1 outlier	III
LB19	099	2.40	14.9 ± 0.6	0.90 ± 0.04	16.6 ± 1.0	OK	Overdispersion16%	III
LB20	100	2.74	13.4 ± 0.5	0.96 ± 0.03	13.9 ± 0.7	OK	Overdispersion12%	III

selected samples, these were density separated at $\rho = 2.58$ kg/dm^3 before treatment with HF to separate K-rich feldspar (light fraction) from other minerals. No HF acid etching was used in the feldspar preparation.

Luminescence measurements were performed on Risoe TL/OSL DA15/20 readers. For equivalent dose measurement on the quartz fraction a SAR protocol (Murray and Wintle, 2003) with 260 °C preheat and 220 °C cutheat was used. Luminescence measurements were for 20s at 125 °C with blue LEDs, and at the end of each SAR cycle the luminescence signal was reset by a 40s blue LED bleach at 270 °C. An early-background approach was adopted to maximize the contribution from the most light-sensitive OSL signal (Cunningham and Wallinga, 2010). Measurements were made on small aliquots (2 mm, ~50 grains). The adopted procedure yielded a dose recovery ratio in excellent agreement with unity (0.99 ± 0.01, $n = 88$). For samples HB6 and HB7 quartz OSL signals were too close to saturation to allow reliable equivalent dose estimation, at least for part of the aliquots.

The palaeodose is the best estimate of the true burial dose, and is obtained through statistical interpretation of the equivalent dose distribution. Based on a combination of the characteristics of the distributions (overdispersion, skewness, outliers) and available information on depositional environment and potential post-depositional disturbances (Wallinga et al., 2019), an appropriate statistical method is selected. For most samples, overdispersion as determined with the Central Age Model (Galbraith et al., 1999) was in line with expectations (<20%). For these samples we based our palaeodose estimate on the mean equivalent dose, after iterative removal of outliers (those estimates deviating more than two standard deviations from the sample mean). For sample HB6 a much broader equivalent dose distribution indicated mixing of grains of different age. As we are interested in the younger component, we adopted a bootstrapped Minimum Age Model (Cunningham and Wallinga, 2012; Galbraith et al., 1999), assuming an overdispersion of 15 ± 3% for this population.

Because quartz OSL signals for two samples (HB6 and HB7) were close to saturation, additional single-aliquot and single grain pIRIR analyses on the feldspar fraction were performed for these samples, as well as single-grain analysis on one additional sample (HB5) for validation. The single-aliquot and single-grain approaches adopted a similar SAR approach (Wallinga et al., 2000; Brill et al., 2018), with a 60s preheat and cutheat at 250 °C, IR stimulation at 50 °C, pIRIR measurement at 225 °C, and additional bleaching at the end of each SAR cycle by a second pIRIR exposure at 225 °C. For the single-aliquot measurements, 200 s stimulation by infrared LEDs was used. Fading was only measured for the single-aliquot approach, results indicated an average fading rate (g value) of 1.45 ± 0.08% / decade. Results are presented without fading correction. Similar to the quartz analysis, we based our palaeodose estimate on the mean equivalent dose after iterative removal of outliers. The single-grain approach used 2 s stimulations by IR laser, and included an additional bleaching step after readout of the natural and regenerative dose. Single-grain dose recovery tests yielded a ratio of ~0.9 for all three samples, which may indicate palaeodose underestimation for this approach. No corrections for this possible underestimation were made. Single-grain analysis for sample HB5 showed a relatively low overdispersion (19 ± 2%), and provided an age which is slightly younger than obtained by quartz OSL. This slight age underestimation may be caused by anomalous fading or relate to the poor dose recovery. Nevertheless, we interpret the similarity of quartz OSL and feldspar pIRIR ages as encouraging. For sample HB7, single-grain and single-aliquot pIRIR results provided similar age estimates, both slightly younger than the (unreliable) quartz OSL age. All results indicate an age of >200 ka. For sample HB6 a clear bimodal distribution was observed in the single-grain equivalent dose distribution, indicating that this sample contains a mix of old sediments (Unit I) and younger deposits (Unit II). A minimum age model (with sigmab 19 ± 2%, based on sample HB5) was adopted to date the young component. The resulting age is much younger than that obtained through quartz OSL, likely due to within-aliquot averaging of equivalent doses with quartz. Hence, the single-grain pIRIR result is regarded most reliable, although a minor underestimation of the age is likely given results on sample HB5.

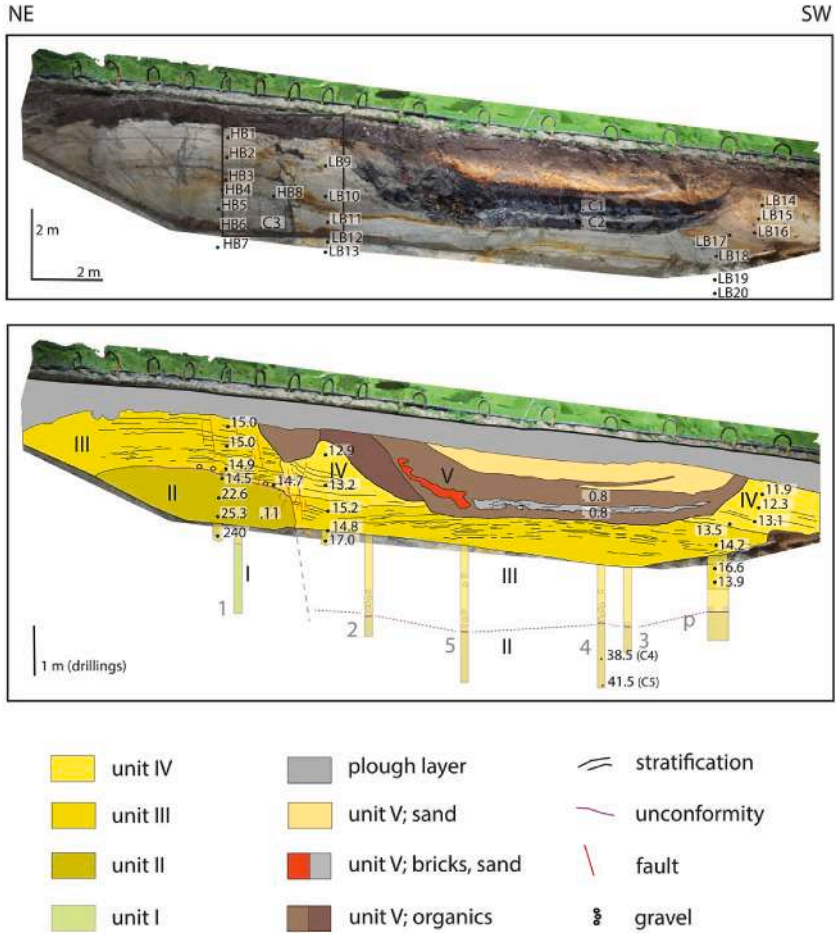

Fig. 5. Southeastern trench wall photo composite (top) and interpretation (bottom). OSL (HB/LB) and ^{14}C (C) sample numbers are on the upper panel, except C4 and C5. Absolute ages are on the lower panel, in ka (OSL) and in calibrated ka BP (^{14}C). Drillings are labeled using large gray numbers; "p" is a larger pit. Red lines indicate faults; the purple line is an unconformity. The rectangle on the upper panel shows the location of Fig. 8a. The northwestern trench wall is depicted in Supplementary Fig. 1. (For interpretation of the references to colour in this figure legend, the reader is referred to the web version of this article.)

3.3. ^{14}C dating

Five samples have been analyzed for ^{14}C dating (Table 2). Two ^{14}C samples, Gr 17,419 and Gr 17,420, have been analyzed at the center for isotope research, Rijks Universiteit Groningen. The ^{14}C ages were calibrated to calendar years using Oxcal v. 4.3 (Bronk Ramsey, 2017) and the calibration curve IntCal13 (Reimer et al., 2013). The probability ranges of the calibrated ages are based on the measuring results and the measurement uncertainty range. In the upper sample pieces of twigs, extracted from the sample material by use of a binocular microscope and subsequently pretreated at the VU, were analyzed; in the lower sample pieces of wood were analyzed. Three ^{14}C samples, Beta-631,298, Beta-631,299 and Beta-631,300, were pretreated and analyzed at the Beta Analytic laboratory (Miami, Florida). The first sample was a root remnant. Both other samples consisted of humic sand. The root fragment was pretreated with acid/alkali/acid. Pretreatment of the humic sand samples consisted of acid washes. The humic sand samples were corrected for $\delta^{13}C$. The results were calibrated using Oxcal v. 4 (Bronk Ramsey, 2009) and the calibration curve IntCal20 (Reimer et al., 2020).

4. Results

4.1. General overview

An aerial overview photo of the trench is depicted in Fig. 4. A panorama photo of the southeastern trench wall is shown in Fig. 5; the northwestern trench wall is depicted in Sup. Fig. 1. At the footwall the average groundwater level is very shallow, over a year varying between about 0.5 to 1 m below the surface. At the hangingwall the average groundwater level varies between 1 and nearly 2 m below surface and

Table 2
Summary of ^{14}C dating results.

Sample	Labcode	^{14}C age (yrBP)	± 1σ	$\delta^{13}C$	Cal. (95.4% prob.)		Unit
C1	Gr 17,419	810	20	−28.75	1191–1266 CE	Twigs	V
C2	Gr 17,420	815	30	−26.84	1168–1266 CE	Wood	V
C3	Beta-631,298	9650	30	−27.5	11,187–11,067 cal BP (54.1%) 10,960–10,866 cal BP (30.4%) 10,852–10,800 cal BP (8.4%) 11,027–11,007 cal BP (2.4%)	Root	II
C4	Beta-631,299	35,420	300	−28.2	39,144–37,894 cal BP	Humic sand	II
C5	Beta-631,300	36,720	360	−28.2	42,089–41,110 cal BP	Humic sand	II

deepens rapidly away from the fault, in line with observations at other parts of the PBFZ (Lapperre et al., 2019, 2022). Two main issues complicate the stratigraphic- and structural interpretations. First, a paleo-channel is exposed in the hangingwall in both trench walls; it is mainly filled with gyttja. The trench cuts the paleo-channel nearly perpendicular, indicating that it is oriented parallel to the fault. The shape of the channel cross-section and the traces of scooping visible at the channel-base show the channel is man-made. As a result of digging the channel, part of the older, pre-channel deposits is missing in the hangingwall. The stratigraphic correlations in the sandy deposits of the hangingwall across the paleo-channel are guided by bedding information in the adjoining (lateral) and underlying geological sequences, and they are supported by dating results. The second issue is that, compared to the sandy deposits exposed in the hangingwall, the corresponding sandy sediments in the footwall overall show reduced colors and contain less silt and organic matter, and they show less clear bedding. The colour difference is explained by differing levels of oxygenation due to difference in groundwater level. The silt and organic matter contents difference is explained by secondary displacement of organic matter and silt by groundwater flow (McDowell-Boyer et al., 1986; Gelet and Marot, 2022). This common observed process is alternatively termed "internal erosion", "migration of fines", "through-wash", and "suffusion" (Horikoshi and Takahashi, 2015; Huggett, 2016; Hicher et al., 2018). The displacement of organic matter is illustrated by the decaying Holocene *Equisetum* roots on the footwall, showing transport in an oblique upward direction (Fig. 6a, b, c). The displaced silt and organic matter has accumulated mainly in and near the main fault zone (Figs. 5, 8; Supp. Fig. 1). The accumulations especially occur next to the main faults, on their footwall side, but they additionally also occur along deformation bands on the hangingwall. The secondary, post-depositional nature of the accumulations is illustrated by the overprinting of sedimentary stratification (Fig. 6a). The fact that the migration of fines and organic matter has mainly occurred on the footwall, and not so much on the hangingwall, is discussed further below (see Discussion section). Below we describe the stratigraphic sequences, taking into account the migration of fines and organic matter. In addition, dating results and cryoturbation structures in Unit II are used to support the stratigraphic correlation between footwall and hangingwall.

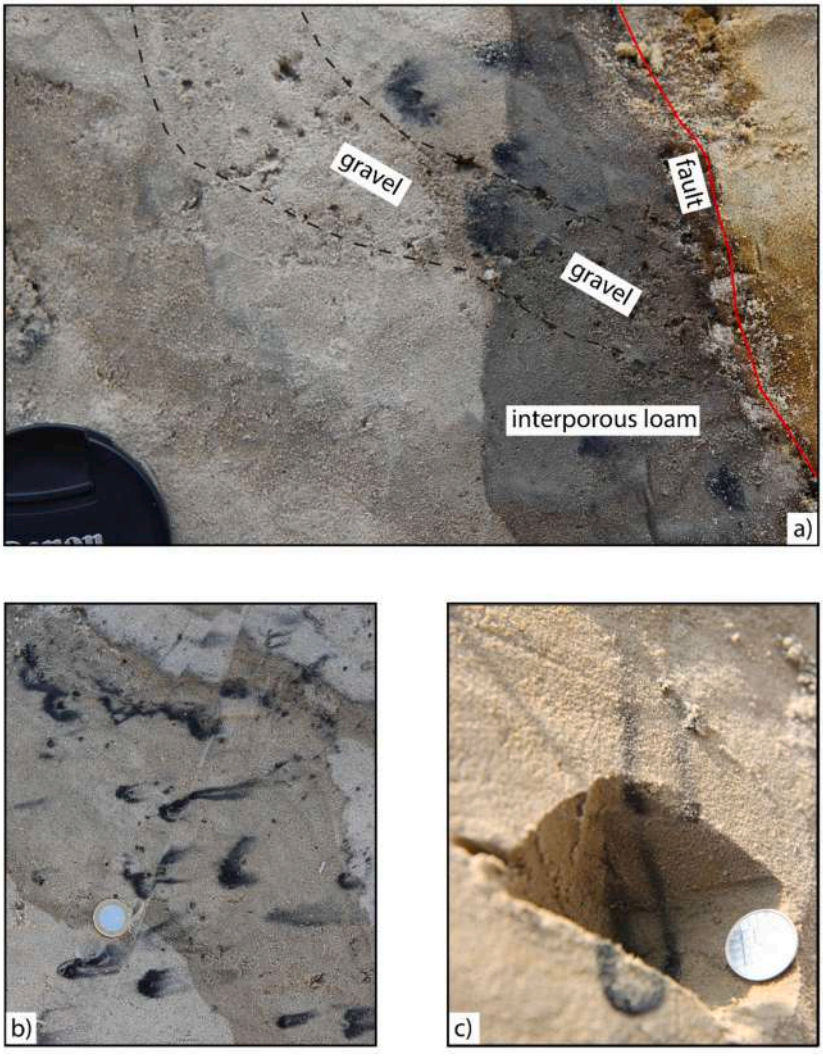

Fig. 6. Examples of displaced organic matter and silt. For locations see Fig. 8.
a) The main fault, secondary accumulation of silt and organic matter (interporous loam) against the footwall side of the fault, overprinting sedimentary stratification indicated by a deformed gravelly sand bed.
b) trails of organic matter from decayed *Equisetum* roots. View at the trench wall, showing a vertical displacements of trails of migrated organic matter by abundant faults with cm's displacement.
c) trails of organic matter from a decayed *Equisetum* root. View from above (the coin lies sub-horizontal). *Equisetum* roots grow vertical. The trails are faulted by one of the many dm-scale faults and show ~1 cm right-lateral displacement.

4.2. Stratigraphy

The sedimentary sequence was exposed in the trench walls, pits dug in the trench floor, and it was inferred from suctions drillings. Based on lithologies, grain-size characteristics, sedimentary stratification (bedding), unconformities, deformation features, drilling results, and OSL and ^{14}C ages (Tables 1, 2), the sequence can be grouped into five units (Fig. 5).

4.2.1. Unit I

This lowermost unit was only observed on the footwall. A ~ 0.8 m thick sequence of this unit was exposed in a pit in the trench floor. It consisted of a 0.5 m thick fining-upward sequence, composed of coarse to medium-sized gray sand with 2 cm sized gravels, overlain by 0.3 m thick, medium-sized and very coarse gray sand, containing mm-sized gravel. A ~ 1.2 m drilled sequence (drilling 1) consisted of coarse to very coarse, gray sand, with 0.3–1.5 cm sized gravel. The gravel contains pebbles of milky quartz, flint, sandstone and quartzite. OSL dating of Unit I (sample HB7; Table 1, Fig. 5) resulted in a likely age of 240 ± 20 ka. Based on the regional geology (Schokker et al., 2007), the coarseness of the deposits, the gravel content, the luminescence age and the overall similarity to Unit A of the Bakel trench (see Setting; Van Balen et al.,

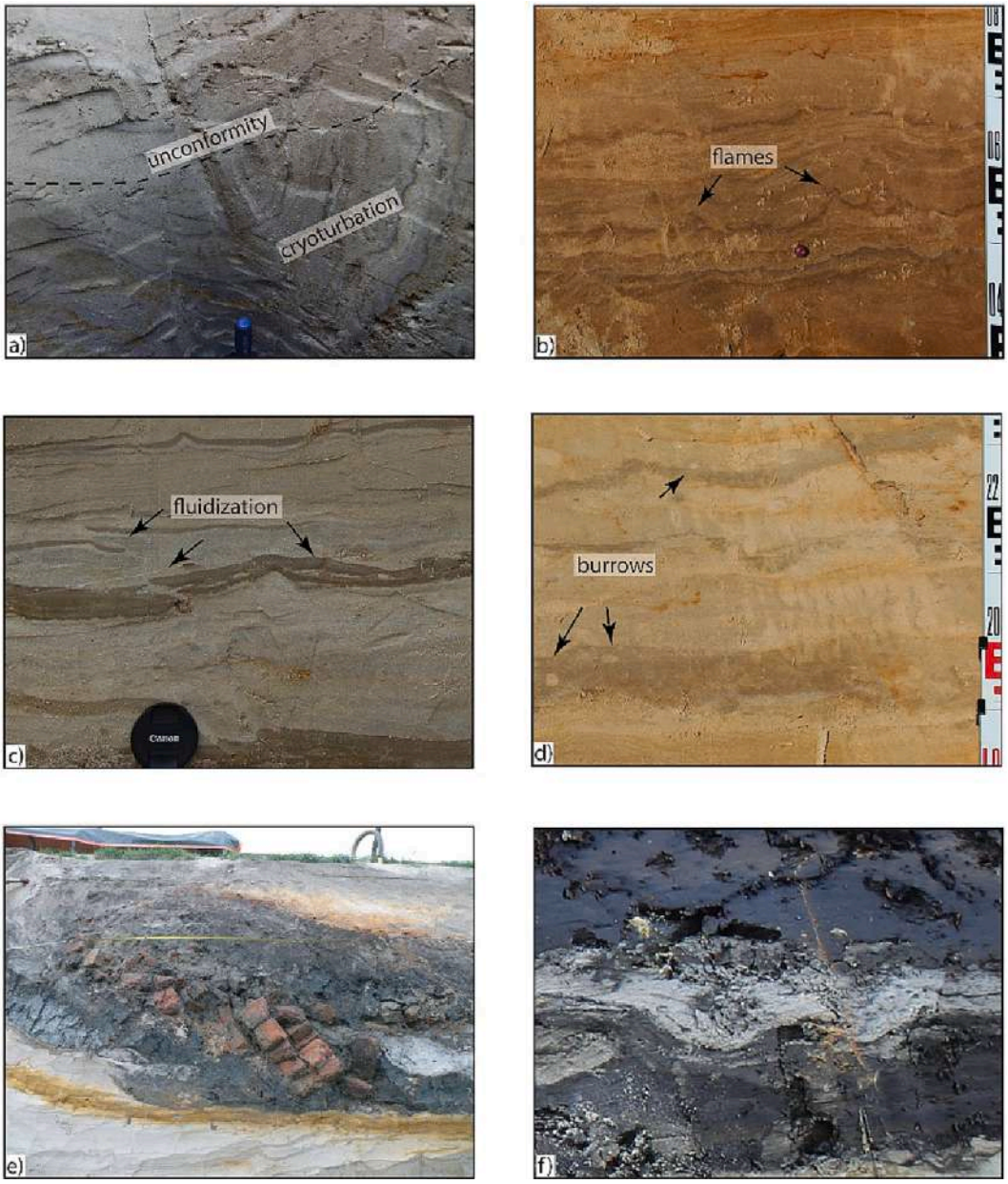

Fig. 7. photo panel showing sedimentary and stratigraphic features.
a) exposure in the larger pit "p" (Fig. 5), showing the unconformity between Units II and III, and cryoturbation of unit II (trowel for scale).
b) flame structures in the top of unit III at the distal part of the trench wall (near pit "p").
c) fluidization in the upper part of unit III, located in between the fault and the infilled man-made paleo-channel.
d) dung beetle burrows characteristic for the well-bedded upper part of Unit IV.
e) collapsed brick-wall in the fault-adjacent flank of the infilled man-made paleochannel (Unit V, Fig. 5). On the right the sand layer depicted in f) can be seen interfingering with the bricks.
f) details of loadings in the sand layer embedded in the basal part of Unit V (Fig. 5). The sand layer is in the same stratigraphic position as the collapsed brick wall (Fig. 7e). The loading deformation is *syn*-sedimentary as the top of the sand layer is hardly deformed.

2019), we interpret the deposits of Unit I as the Beegden Formation, a fluvial deposit formed by the Meuse river. In the Bakel trench the Beegden Formation was dated to 286 ± 25 to 262 ± 24 ka. Based on core data archived at the geological survey, the top of the unit is located at a depth of about 20 m on the hangingwall (www.dinoloket.nl).

4.2.2. Unit II

On the footwall, this unit consists of a ~ 1 m thick alternation of white-gray fine sand, loamy fine sand, loamy sand, sand with small gravels, and gravelly sand (gravel size up to 1 cm). The loam content increases upwards. Overall, the unit appeared strongly homogenized; stratification occurs near the basal part of the unit, next to the fault, but lacks in other parts of the unit. One deformed, layer-like concentration of gravel (dispersed in the sand matrix) occurred in the middle of the unit (Fig. 6a). The basal 0.2 m consisted of dark brown, humic coarse sand (in a trench floor pit and in drilling 1). Next to the fault, the top of Unit II is eroded and is onlapped by Unit III.

On the hanging wall Unit II was not exposed in the trench walls. A temporary pit in the trench floor showed a strongly deformed sequence of gray loamy fine sand, and dark brown, humic- and gravelly sand (Fig. 7a). The overlying Unit III was not deformed. Drilling 2 showed 0.4 m of dark-brown, humic, coarse sand with gravel. In drilling 5, the unit consisted of a 0.65 m thick alternation of layered, brown, humic sand and gray sand; at the base of the drilling parts of peat were drilled-up. In drilling 4, the 1.75 m thick drilled sequence consisted of gray, medium sized humic sand, with some gravel and, at the base, very dark brown, humic, medium sized sand. In drilling 3, a 0.5 m thick humic medium sized sand with gravel (size 3 mm) was found. In summary, on the hangingwall Unit II consisted of an at least 1.75 m thick alternation of dark brown humic and non-humic sand, with 3 mm sized gravel and organics (humic sand and peat).

An age of ~40 ka is inferred for the base of the unit, based on ^{14}C ages for humic sand from the hangingwall (base of drilling 4; lab. Numbers Beta-631,299 and -631,300; Table 2). Note that these dates approach the limit of the ^{14}C method. Luminescence ages (Table 1, Fig. 5) in the middle part of the unit on the footwall are ~25–22 ka (samples HB6 and HB5), whereas the top (sample HB4) is ~14.5 ka. The luminescence age of sample HB4 seems relatively young, which hints at bioturbation or another kind of disturbance in the top of the unit. There are however no indications for soil formation nor signs of imperfect bleaching or mixing of sediment. In addition, the concentrations of radionuclides in samples HB4 and HB5 are similar, indicating that they indeed belong to the same depositional unit. According to the ^{14}C ages, the basal sediments of Unit II on the hangingwall are of Weichselian Middle Pleniglacial age. Luminescence ages show that the main part of Unit II, however, correlates to the Weichselian Upper Pleniglacial Older Coversand I deposits (Kasse et al., 2007).

4.2.3. Unit III

This unit is composed of a coarse grained lower part and a finer grained upper part. On the footwall, the coarse lower part consists of a layer of cm-sized gravels. Close to the fault it lies unconformably on Unit II. On the hangingwall, the coarse lower part was not exposed. In drillings and in a pit in the trench floor it consisted of coarse and medium sized sand with large gravels (2.5 cm). The thickness decreased from 0.60 m to 0.20 m in the direction away from the fault, indicating a wedge shape.

On the hanging wall, the finer upper part is about 1.5 m thick; the thickness decreases slightly in the direction away from the fault. It comprised an alternation of gray and whitish coarse gravelly sand, medium-sized sand, fine sand and loamy fine sand, with an overall fining upward trend. Stratification is at mm and cm scale. Beds of small (mm) gravels occurred throughout this part of the unit. Near the base, small gravel concentrations occur in troughs and ripples. On the footwall the fine upper part of Unit III was around 1 m thick. Here the unit showed much less stratification, due to the groundwater erosion/suffusion process. It consisted of an alternation of layers of fine and coarse sand and beds of gravel (mm).

Luminescence samples taken on the footwall resulted in ages of around 15 ka (Table 1, Fig. 5). Samples from the hangingwall taken close to the fault (LB11, −12, −13) and at the distal part of the trench (LB18, −19, and − 20) resulted in similar ages. Based on the age, facies and lithologies, Unit III corresponds to the Upper Pleniglacial Older Coversand II unit (Kasse et al., 2007).

4.2.4. Unit IV

This unit is exposed on the hangingwall and does not occur on the footwall. It consists of cm's thick loamy sand and sand beds; the thicknesses of the beds increases upwards. In contrast to underlying Unit III, the deposits of this unit lack gravel. Another important contrast with underlying Unit III is that the sand and loam beds are much thicker, which indicates bioturbation. In some loamy sand beds dung beetle burrows were encountered (Fig. 7d). The sand bed overlying the uppermost loamy sand bed is bleached, likely due to a soil formation process.

Close to the fault, Unit IV overlies Unit III discordantly (Fig. 5; Supp. Figs. 1, 2). In addition, the concave upward bedding towards the fault suggests that it has been deposited against a paleo-fault scarp, which is furthermore indicated by the decreasing thickness away from the fault, from at least 1.0 m (top eroded) to 0.70 m. In the southwestern distal part of the trench Unit IV overlies Unit III concordantly and flame structures are present near their contact in underlying Unit III (Fig. 7b).

Luminescence ages of Unit IV vary between ~14 and 12 ka (samples LB9, −10, −14, −15, −16 and − 17; Table 1, Fig. 5). Unit IV has ages and facies characteristics indicating that it can be correlated to the Late Glacial Younger Coversand I and II series (Kasse et al., 2007). The bleached horizon and burrows could indicate the Allerød Usselo soil, which usually separates these series. However, the characteristic charcoal particles of this soil (Van Hoesel et al., 2012) have not been encountered in this trench.

4.2.5. Unit V

This unit consist of the infill of a paleo-channel. Because of its cross-sectional shape and the scoop traces at the bottom, the channel is man-made. The channel is located on the hangingwall, while an associated smaller ditch feature overlies the fault zone. The main channel-filling component is gyttja. The fill contains siderite concretions, vivianite, and abundant archeological remains, like pottery, bricks, iron slags and parts of a shoe sole (Hiddink, 2019). Part of the bricks occur interconnected; they represent the remnants of a wall (Fig. 7e).

At the base of the fill sequence the gyttja is layered: greenish and whitish gyttja layers occur interbedded with a massive dark gray gyttja layer. These basal gyttja deposits contain abundant leaf and twig fragments. A ~ 25 cm thick coarse sand layer with humic fragments overlies the basal gyttja. This sand layer shows loading structures (Fig. 7f), which must have formed while the sand layer was deposited, since the top of the layer is less deformed than the base. A second, darker colored and more massive gyttja overlies the sand layer. This gyttja layer is in turn overlain by orange colored, medium sized sand. All the gyttja layers transition laterally into sand at the sides of the paleo-channel.

The pollen assemblage of the gyttja is dominated by *Alnus* (Van der Woude and Van Leeuwen, 2020). The presence of wheat pollen (especially *Fagopyrum*, buckwheat) points at a Medieval age (1250–1500 CE). The calibrated ^{14}C dating results for the upper part of the fill (sample Gr 17,419, twig) is 1191–1266 CE; the lower part of the fill (sample Gr 17,420, wood fragment) is dated to 1168–1266 CE (Table 2; Hiddink, 2019). The channel fill thus dates from the first half of 13th century. The pottery remains and brick type roughly have a 14th century age. Since they are younger, they must have become part of the channel fill at a later stage, as waste (Van der Woude and Van Leeuwen, 2020). However, the bricks of the wall remnant are related to the loadings of the coarse sand layer, and thus have the same age as the channel fill.

4.2.6. Holocene roots

Units II and III on the footwall contain the remains of decaying roots. Judged from their shape and length these are likely *Equisetum* roots. These roots have grown vertically, but are now displaced by a bundle of minor faults. The organic matter produced by the decay process is present in the pores of two zones diverging away from the root remains (Fig. 6b,c). As presented before, this evidences organic matter transport through the pores by oblique upward directed groundwater flow.

^{14}C dating of the root remnants results in an age range of 11,187 to 10,800 cal BP (95.4% probability; sample number Beta-631298; Table 2).

4.3. Structural observations

In the trench a ~ 3 m wide fault zone was exposed, consisting of a fault core and a damage zone composed of multiple minor faults. The fault zone is asymmetric; the largest width (~2 m) occurs on the footwall (Fig. 5). The displacement is mainly concentrated at one, sharply delineated fault core. This core has a width varying between 3 and 15 cm's and consists of sediment (silt, sand, and a few small gravels) mixed by displacement, lacking sedimentary stratification, thus presenting a fault gouge in non-consolidated sediment. The faulting displaces Units I to IV, but the base and the infill of the man-made paleo-channel, Unit V, is not faulted (Fig. 5; Supp. Fig. 3). In the southeastern trench wall the fault core dips 210/60 (steepening upward; the apparent dip on Fig. 5 is due to photographic distortion). At the northwestern trench wall (Supp. Fig. 1), the upper part of the fault core is overturned and it is splayed; dips vary between 030/80 to 035/85. Overturning is a common feature observed in many trenches in the RVRS (Houtgast et al., 2005; Camelbeeck et al., 2007; Vanneste et al., 2013; Grützner et al., 2016; Verbeeck et al., 2017; Van Balen et al., 2019). It is explained by a decrease of confining pressure towards the surface during a rupturing event in unconsolidated sediments (McCalpin, 2009; Vanneste et al., 2013; Verbeeck et al., 2017). Earthquake focal mechanism data show that, at depth, the PBFZ has a southwestern dip of around 60 degrees (Vanneste et al., 2013; Hinzen et al., 2021).

The minor faults in the ~3 m wide fault zone consist of *syn*- and antithetic faults with cm's displacement (Figs. 5, 8; Supp. Figs. 1, 2, 3), which affect all pre-channel deposits. Synthetic faults dominate, and result in a total offset across the fault zone of about 0.2 m. They show no evidence for growth faulting, implying there has been only one single faulting episode for these minor faults. The Holocene *Equisetum* roots, situated in Units II and III on the footwall, are offset by the minor faults, with dm's displacement (Fig. 6 b, c). In addition to the normal faulting component, the roots are offset with a right-lateral displacement component, with cm's displacement (Fig. 6c). The 13th century man-made paleo-channel (Unit V), is not affected and thus post-dates the minor faulting.

Flame structures (i.e. upward-directed, intraformational, cm-scale fold structures) occur in the upper part of Unit III (Fig. 7b), near the contact with Unit IV, in the southeastern trench wall, on both sides of the man-made paleo-channel. Close to the fault zone other fluidizations occur at the same stratigraphic level (Fig. 7c). The vertical displacement of the top of Unit III is at least 1.25 m, whereas the vertical offset of the top of underlying Unit II is 2.45 m. Units III and II show no evidence for growth faulting.

5. Discussion

5.1. Migration mechanism

The sediments on the footwall have experienced migration of silt and organic matter by groundwater flow. The migration process requires sufficient pore space, which in turn depends on the size of the grains,

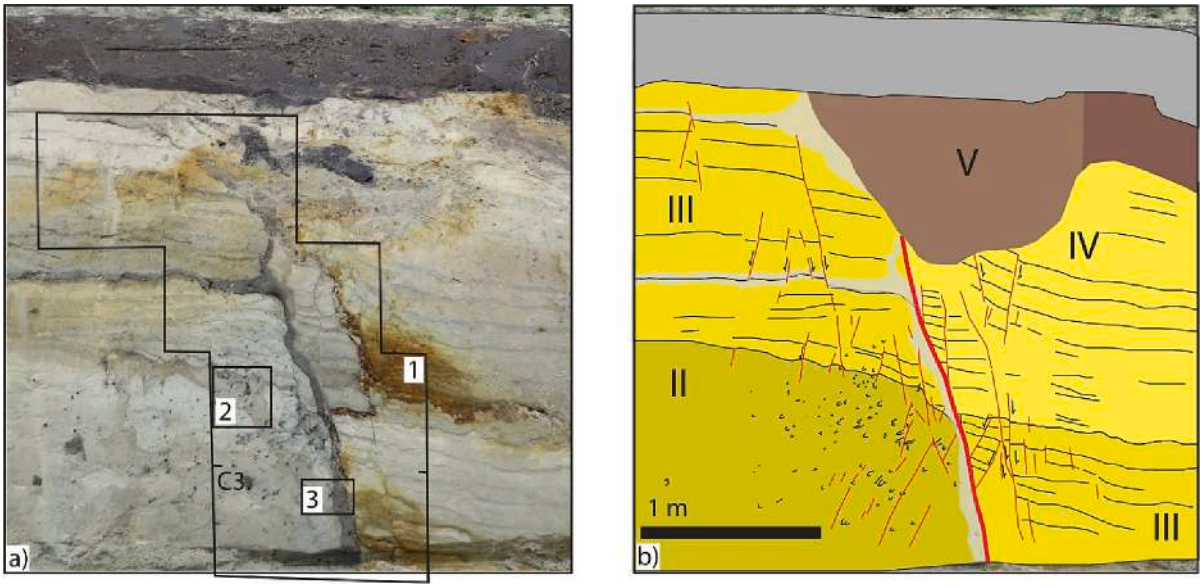

Fig. 8. Close-up of the fault zone.
a) Fault core and damage zone of the southeastern trench wall. The position of this figure is shown by a rectangle in Fig. 5, upper panel. Rectangle 1) indicates the location of the lacquer peel depicted in Supplementary Fig. 3. Rectangle 2) depicts the location of Fig. 6b; rectangle 3) positions Fig. 6a. "C3" is a ^{14}C sample, dating a decayed root (also indicated on Fig. 5).
b) interpretation of a). Red lines are faults, the thicker one is the main fault.
The main fault has affected all units, except the infill of the man-made paleochannel, Unit V. The minor faults have been mapped using also Supplementary Fig. 3. The minor faults postdate Unit IV and the organic matter trails, but predate Unit V. The minor faults occur in synthetic and antithetic directions, have small individual displacements, and a small total vertical offset despite their large number.
Silt and organic matter has migrated towards the fault and towards a few prominent (litho-)stratigraphic boundaries. These accumulations are indicted with a light gray colour on Fig. 8b. For other items see legend of Fig. 5. Small parabolic marks in Units II and III on the footwall represent organic matter trails from decayed *Equisetum* roots, indicating oblique upward groundwater flow. These trails are faulted (Fig. 6). (For interpretation of the references to colour in this figure legend, the reader is referred to the web version of this article.)

their form, and the fabric (Horikoshi and Takahashi, 2015; Hicher et al., 2018; Gelet and Marot, 2022). Originally, these sediment properties were the same at the footwall and hangingwall, and thus they cannot explain the difference in internal erosion between the two sides of the fault. Groundwater flow rate differences can also not explain the difference in internal erosion, as the groundwater flow system across the fault zone is essentially two-dimensional, and the flow rates at both sides of the fault are similar (Lapperre et al., 2022). The main hydrological difference between the footwall and hangingwall is the average groundwater level (Lapperre et al., 2019, 2022): At the footwall the groundwater level is near the surface, with sometimes even seepage occurring, whereas on the hangingwall it is located at depth. This difference is important during past cold-climatic conditions, because the higher groundwater level causes the footwall to be more susceptible to cryogenic alteration due to formation and melting of ice-lenses, ice needles, etc. (French, 2017; Zhong et al., 2020). Thus, the silt and organic matter mobilization can potentially be explained by the combined effects of freezing and melting processes (the latter lead to fluidization of the active layer sediments upon melting). The transport of silt and organic matter by groundwater is towards the hangingwall, in the direction of the topographic gradient, but it is blocked by the fault structures due to their low permeability, as a result of clay smear, grain-reorientation, juxtaposition, and iron-oxide precipitation (Lapperre et al., 2019, 2022). This causes accumulations of silt and organic matter in the sediment pores, mainly at the footwall side of the fault structures, which further reduces fault permeability, and causes more trapping of silt and organic matter.

5.2. Minor fault structures

Apart from a principal fault, the fault zone contains abundant, distributed minor faults in the damage zone at both sides of the main fault. They represent the youngest deformation event, which has taken place during the Holocene, because of the displaced *Equisetum* roots, and before the excavation of the 13th century man-made channel (Unit V). The numerous faults have synthetic and antithetic orientations, and their individual displacements are only a few centimeters (Figs. 5, 8; Supp. Fig. 1). The net vertical displacement of the dozens of minor faults across the fault zone is only in the order of 0.2 m and the fault core is hardly affected by them. Such a distributed faulting has not been observed in previous trenches in the RVRS, and in this trench it only occurred during the latest time-interval, since all units except Unit V, the infilled man-made channel, are affected by it by the same amount.

Digging of the channel cannot explain the faulting, because the channel is unaffected and the depth-extent of the faults is well below the base of the man-made channel. Gravitational collapse of the fault scarp can also not explain the minor faulting, because there is hardly any net vertical displacement, the faults are straight and not concave, slump-like, and thrusts evidencing mass-movement are lacking further downslope (e.g. Houtgast et al., 2005). The minor faults could, however, represent a negative flower structure created by transtensional motions along this segment of the PBFZ, which is indicated by the right-lateral displaced *Equisetum* roots (Fig. 6c). Although the dominant displacement mode in the RVRS is normal faulting, strike-slip motions do occur, as evidenced by earthquakes in the RVRS: About one third of the focal mechanisms have nodal planes with a strike-slip motion (Hinzen et al., 2021).The displacement style for faults in the RVRS inferred from tectonic morphology and trenching results is pure normal faulting (Van Balen et al., 2005, 2019, 2021; Michon and Van Balen, 2005; Woolderink et al., 2019). However, according to Vanneste et al. (2013), the faulting mode inferred from trenching results might be biased by the orientation of the faults studied in trenches thus far. Furthermore, strike-slip motions can be expected because the extension direction in the RVRS is (slightly) oblique (Michon et al., 2003; Worum et al., 2004, 2005; Vanneste et al., 2013). However, because of its orientation with respect to the NW-SE directed maximum horizontal stress direction (Müller et al., 1992), the displacement along the PBFZ should have a left-lateral shear component, which contrasts with the right-lateral displacement of the roots. As an alternative, the right-lateral displacement can be explained by local conditions. For example, it could be the effect of the tip of a (normal faulting) rupture segment (Choi et al., 2016) with an epicenter located to the NW. Or it could be the result of a change in fault strike. However, we have no further indications to constrain these hypotheses. Finally, the lateral faulting component can potentially be explained by the glacio-isostatic triggering mechanism for faulting events, see section 5.3.2. The asymmetry of the width of the damage zone, which is ~2 m wide on the footwall and ~ 1 wide on the hangingwall, can be explained different sediment properties across the fault (Choi et al., 2016), since the coarse grained and therefore relatively strong unit I observed in the trench at the footwall is buried at ~20 m depth at the hangingwall.

5.3. Displacements, (paleo-)scarps and wedges

All units except Unit V are effected by the 0.2 m net displacement of the most recent, possibly trans-tensional event. The preceding displacements events can be inferred using stratigraphy, inferred paleo-topography, and fluidization features.

Aeolian Unit IV was deposited against a scarp, because this unit is not present on the footwall, its internal stratification is directed upwards towards the fault, and its thickness decreases away from the fault. However, there was no scarp during deposition of the upper part of underlying Unit III, because its internal stratification on both the footwall and hangingwall shows no evidence for it (Fig. 5). The scarp was thus created in the short time span between deposition of Units III and IV, around ~14 ka. Furthermore, fluidization features occur in the top of Unit III, on the hangingwall, close to the contact with overlying Unit IV. The contact between Units III and IV is thus an event layer. The top of Unit III has an offset of 1.25 m. Due to potential erosion on the footwall and/or uptake in the plough layer, the fault displacement of the top of Unit III can in theory have been larger. However, the unit is only 0.5 m thicker on the hangingwall, which can be explained by the onlapping nature of Unit III on the footwall (Unit III drapes a scarp created by an older event, see below), resulting in less total thickness at the footwall. The Recent footwall erosion and or ploughing effects are thus minor. The fault displacement resulting in the scarp against which Unit IV was deposited was thus about 1.25 m minus the 0.2 m offset of the younger event, resulting in ~1.05 m. The displacement indicates a surface rupturing earthquake with a magnitude Mw of about 7 (Wells and Coppersmith, 1994; Trippetta et al., 2019).

The coarse grained basal part of Unit III on the hangingwall is interpreted to be a colluvial wedge. On the footwall it corresponds to the erosional unconformity between Units II and III. The base of Unit III is thus interpreted to be an event layer. Unit II consists of sand, silt and peat, which indicate low energetic conditions during deposition. This suggests that no significant fault scarp was present at this site during formation of Unit II. The total offset of the base of Unit III/top of Unit II is 2.45 m, which is the sum of the two younger events and the fault displacement taking place following the deposition of Unit II (and before deposition of Unit III). This fault displacement event was thus 1.2 m (2.45–1.25). The reconstructed fault displacement was likely abrupt, because evidence for growth faulting is lacking and the combination of an erosional unconformity with a colluvial wedge, both with energetic conditions sufficiently large for transport of 2.5 cm sized pebbles, evidence abrupt relief. The displacement indicates a similar surface rupturing earthquake like the younger event, with a magnitude Mw of about 7. The timing of this event is ~15 ka, based on the OSL dating results of Units II and III and considering that deposition of Unit III should take more time than 500 years, we use the upper limit of the dating result of OSL sample HB4.

The total offset observed in this trench, 2.45 m, is larger than in the previously studied trenches at the PBFZ. However, it is in agreement

with the larger present-day scarp height and the thicker Miocene to recent *syn*-rift deposits at this location, which both indicate a larger fault offset compared to other locations along the PBFZ (Fig. 2b). In addition, the total offset of 2.45 m is in line with the 2.30 m displacement of the Late Pleniglacial terrace, buried by Holocene Rhine-Meuse deposits, in the adjoining area located northwest of the study site (Cohen et al., 2002). The timing of the major surface rupturing events (~15 ka and ~ 14 ka) suggests a close relation to glacio-isostatic movements in the RVRS, like in the previous trenching studies (Houtgast et al., 2005; Van Balen et al., 2019, 2021).

The oldest unit on the footwall (Unit I, ~240 ka) is located at a depth of about 20 m on the hangingwall (see 4.1.1). The long time interval between deposition of Units I and II precludes assessment of faulting events. The long term fault displacement rate since the deposition of this unit is about 20 m / 240 ky = 0.08 mm/y.

5.3.1. *Reconstruction of events*

Based on the inferences above, the following reconstruction can be made: During the deposition of Unit II no scarp was present (Fig. 9a). The first prominent scarp formed at the transition from Unit II to III, at ~15 ka (Fig. 9b). The scarp was subsequently eroded and a colluvial wedge formed at the hangingwall. The scarp and wedge were blanketed by the rest of Unit III (Fig. 9c). Following deposition of Unit III, a new scarp was formed at ~14 ka (Fig. 9d). We find no evidence for erosion of this scarp and also a colluvial wedge on the hangingwall is lacking. Instead, the scarp relief is levelled by deposition of Unit IV on the hangingwall (Fig. 9e). This unit was formed by dry aeolian sedimentation. Therefore, absence of surface runoff may explain the lack of scarp erosion. Following this phase of deposition, the third event caused the abundant cm-scale faulting (Fig. 9f). The inferred transtensional faulting event took place during the Holocene, before the construction of the man-made channel in the 13th century (Fig. 9g). Indications for a fourth, non-surface rupturing event are found in the infill of the man-made paleo-channel. They consist of a collapsed brick wall, and additional separated bricks, which suggest, given the context of a seismically active fault, collapse by seismic shaking (Fig. 9g). Loadings in a coarse sand layer embedded in Unit V will have been triggered by the same shaking event, as the intensity of loading deformations decreases away from the brick wall. Age constraints available for the gyttja deposits can be used to situate this earthquake event in the first half of the 13th century. After this event, the man-made channel became completely filled (Fig. 9h). We have not been able to find this earthquake event in records of historic earthquakes (e.g. Houtgast, 1991; Alexandre, 1994).

5.3.2. *Triggering mechanism*

Like in previous trenching results in the RVRS (Houtgast et al., 2005; Van Balen et al., 2019, 2021), the timing of the two oldest, large events, ~15 ka and ~ 14 ka suggests a relation with glacio-isostatic adjustment (GIA). The timing of these faulting events is in agreement with independent evidence for a forebulge and its collapse based on sea-level data

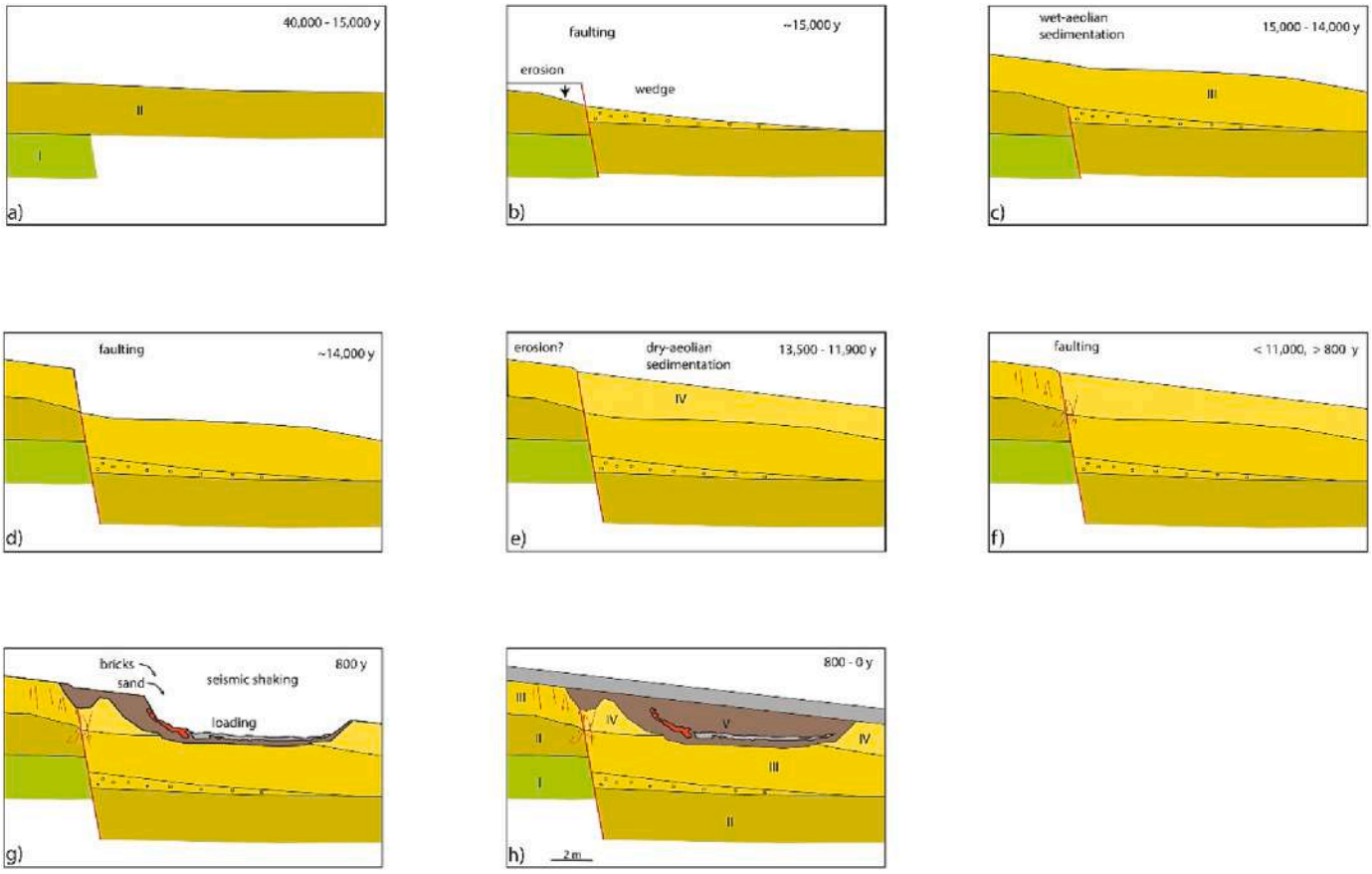

Fig. 9. Schematic reconstruction of events.
a) Following the deposition of Unit I by the Meuse river, loamy Unit II was formed, with one or more cycles of sedimentation, erosion, soil formation and cryoturbation. b) Around 15 ka, a first large surface rupturing event took place, subsequently followed by footwall erosion, and deposition of a clastic wedge at the hangingwall. c) The landscape was blanketed by (mainly aeolian) deposition of sandy and loamy Unit III. d) This unit was faulted by a second surface rupturing event at ~14 ka. e) deposition of sandy aeolian Unit IV against the scarp. f) minor faulting by distributed faults during the Holocene, pre-dating the infill of the man-made channel. This event was also surface rupturing, but the total vertical displacement was limited to ~0.2 m. Laterally displaced trails of organic matter (resulting from decayed roots) indicate transtensional faulting. g) Finally, a likely fourth event is witnessed by a collapsed brick-wall and loadings in a sand deposit embedded in the organic infill of a man-made channel (Unit V).

(Kiden et al., 2002), fluvial response of the Rhine river (Busschers et al., 2007) and GIA-modelling (e.g. Craig et al., 2023). Forebulge decay causes additional stresses which may stimulate the slip of faults, depending on their orientation and on the ambient plate-tectonic stress conditions (Hampel et al., 2009; Craig et al., 2023; Damon et al., 2023). According to the modelling results of Craig et al. (2023), GIA may be another alternative to explain the right-lateral displacement of the Holocene surface rupturing event (their Fig. 4e, f).

5.4. Rupture lengths

The maximum rupture length of surface rupturing earthquakes at the PBFZ can be calculated theoretically based on the seismogenic thickness of the crust. The ratio of surface rupture length to rupture width (the thickness of seismogenic layer) is similar for all earthquake sizes; It ranges from 1 to 3, averaging around 1.6 (Stock and Smith, 2000; Thingbaijam et al., 2017). Because the maximum rupture width equals the thickness of the seismogenic layer, which is around 25 km in the RVRS (Vanneste et al., 2013; Grützner et al., 2016; Hinzen et al., 2021), the theoretical maximum rupture length is 25–75 km, and averages at about 40 km. This in agreement with a rupture length of about 55 km inferred for the Erft/Swift fault (located in the German part of the RVRS; Vanneste et al., 2013); and a rupture length of 11.5 to 28 km for part of the Feldbiss Fault zone (FFZ) (based on trenching results; Camelbeeck et al., 2007).

A maximum rupture length of 25–75 km is much shorter than the 125 km length of the PBFZ, indicating that it likely consists of multiple rupture segments. Also the structural complexity of the PBFZ, consisting of fault bifurcations, fault orientation changes and step-overs (e.g. Michon and Van Balen, 2005)., indicates that multiple rupture segments are likely present (Wesnousky, 2006; Vanneste et al., 2013). Previously we have estimated a minimum length of 35 km for the oldest surface rupture event in the Bakel and Neer trenches (Van Balen et al., 2019). The results from the Uden trench show that this event can also be correlated (Table 3), resulting in a minimum rupture length of 55 km (the distance between the Uden and Neer trenches).

6. Conclusions

The paleoseismic activity of the Peel Boundary Fault zone has been studied in a new trench, located at the maximum *syn*-rift depocenter and scarp heights. Three to four earthquake events were reconstructed. The oldest event occurred around 15 ka, and had 1.2 m displacement, translating into Mw ~7. A second, similar magnitude event, with 1.05 m displacement, occurred at about 14 ka. Both events were surface rupturing, normal faulting earthquake events, as furthermore evidenced by (colluvial) wedges and fluidizations and a lack of growth faulting. The timing of both events suggest that glacio-isostatic adjustment is the triggering mechanism. The third event occurred during the Holocene. In contrast to the two older events, it is characterized by numerous, small-scale syn- and antithetic faulting. It causes the fault zone to be 3 m wide. Despite the abundance of small faults, the net vertical displacement during this event was only about 0.2 m. It is interpreted as a trans-tensional event, which is supported by the observed right lateral displacement of trails of organic matter from decayed roots. A likely fourth event took place during the first half of the 13th century. It is inferred from loading deformations and a collapsed brick wall preserved in the infill of a man-made channel on the hanging wall. A minimum rupture length of 55 km for one of the older events is inferred from a correlation to previous trenching results. This rupture length and the fault offset in agreement with findings elsewhere in the RVRS and the theoretical maximum earthquake magnitude based on the seismogenic thickness of the crust, and with the magnitude-frequency distribution of instrumental earthquakes. The timing of the first two main events suggests a relation to glacio-isostatic motions.

Table 3
Proposed correlation of trenching results. Timing and displacements of events are listed. The results for Uden are based on this work. The results for Bakel and Neer are after Van Balen et al. (2019). The youngest event in Bakel and Neer has not been dated exactly, but likely took place during the last part of the Allerød time-period (13.9–12.9 ka; Van Balen et al., 2019). In the Uden trench there is no evidence for an Allerød event. The correlation results show that the three trenches can be located on the same 55 km long rupturing segment for the ~14 ka event.

Age/Trench	Uden	Bakel	Neer
13th century	0 m	x	x
Holocene	0.2 m	x	x
~13 ka	x	0.10–0.20 m	0.35 m
~14 ka	1.05 m	0.95–1.05 m	0.50 m
~15 ka	1.20 m	x	x

CRediT authorship contribution statement

R.T. Van Balen: Writing – original draft, Visualization, Methodology, Investigation, Conceptualization. **R.E. Lapperre:** Writing – review & editing, Investigation, Conceptualization. **H.A.G. Woolderink:** Writing – review & editing, Investigation. **J. Wallinga:** Writing – review & editing, Methodology, Investigation. **C. Kasse:** Conceptualization, Investigation, Writing – review & editing.

Declaration of competing interest

The authors declare that they have no known competing financial interests or personal relationships that could have appeared to influence the work reported in this paper.

Data availability

Data will be made available on request.

Acknowledgements

We thank landowners Hans and Christa de Bruin to allow the excavation of the trench on their property. Furthermore, we thank Mark Kerkhoff (formerly at Waterboard Aa and Maas), Thea Huijsmans, Erik Heskes (Province of Noord-Brabant) and Jon Mensink for their support. Finally we thank the anonymous reviewer and Klaus Reicherter for their efforts.

Appendix A. Supplementary data

Supplementary data to this article can be found online at https://doi.org/10.1016/j.tecto.2024.230322.

References

Alexandre, P., 1994. Historical seismicity of the lower Rhine and Meuse valleys from 600 to 1525: a new critical review. Geol. Mijnb. 73, 431–438.
Bazelmans, J., Van Balen, R., Bos, J., Brinkkemper, O., Colenberg, J., Doeve, P., Van Geel, B., Hakbijl, T., Van Hateren, H., Hoek, W.Z., Huisman, H., Jansma, E., Kasse, C., Van Os, B., Van der Plicht, H., Schokker, J., Van der Putten, N., Van der Woude, J., 2021. Environmental changes in the late Allerød and early Younger Dryas in the Netherlands: a multiproxy high-resolution record from a site with two Pinus sylvestris populations. Quat. Sci. Rev. 272, 107199.
Brandes, C., Winsemann, J., Roskoch, J., Meinsen, J., Tanner, D.C., Frechen, M., Steffen, H., Wu, P., 2012. Activity of the Osning thrust in Central Europe during the Lateglacial: ice-sheet and lithosphere interactions. Quat. Sci. Rev. 38, 49–62.
Brandes, C., Steffen, H., Steffen, R., Wu, P., 2015. Intraplate seismicity in northern Central Europe is induced by the last glaciation. Geology 43, 611–614.
Brandes, C., Streffen, H., Sandersen, P.B.E., Wu, P., Winsemann, J., 2018. Glacially induced faulting along the NW segment of the Sorgenfrei-Tornquist Zone, northern Denmark: implications for neotectonics and Lateglacial fault-bound basin formation. Quat. Sci. Rev. 189, 149–168.
Brill, D., Reimann, T., Wallinga, J., May, S.M., Engel, M., Riedesel, S., Brückner, H., 2018. Testing the accuracy of feldspar single grains to date late Holocene cyclone

and tsunami deposits. Quat. Geochronol. 48, 91–103. https://doi.org/10.1016/j.quageo.2018.09.001.
Bronk Ramsey, C., 2009. Bayesian analysis of radiocarbon dates. Radiocarbon 51, 337–360. https://doi.org/10.1017/S0033822200033865.
Bronk Ramsey, C., 2017. Methods for summarizing Radiocarbon Datasets. Radiocarbon 59, 1809–1833.
Busschers, F.S., Kasse, C., Van Balen, R.T., Vandenberghe, J., Cohen, K.M., Weerts, H.J.T., Wallinga, J., Johns, C., Cleveringa, P., Bunnik, F.P.M., 2007. Late Pleistocene evolution of the Rhine in the southern North-Sea Basin: imprints of climate change, sea-level oscillations and glacio-isostacy. Quat. Sci. Rev. 26, 3216–3248.
Camelbeeck, T., Vanneste, K., Alexandre, P., Verbeeck, K., Petermans, T., Rosset, P., Everaerts, M., Warnant, R., Van Camp, M., 2007. Relevance of active faulting and seismicity studies to assessments of long-term earthquake activity and maximum magnitude in intraplate northwest Europe, between the Lower Rhine Embayment and the North Sea. In: Stein, S., Mazzotti, S. (Eds.), Continental Intraplate Earthquakes: Science, Hazard and Policy Issues. Geological Society of America Special Paper, 425, pp. 193–224.
Choi, J.H., Edwards, P., Ko, K., Kim, J.S., 2016. Definition and classification of fault damage zones: a review and a new methodological approach. Earth Sci. Rev. 152, 70–87. https://doi.org/10.1016/j.earscirev.2015.11.006.
Cohen, K.M., Stouthamer, E., Berendsen, H.J.A., 2002. Fluvial deposits as a record for late Quaternary neotectonic activity in the Rhine-Meuse delta, the Netherlands. Netherlands J. Geosci. - Geologie en Mijnbouw 81, 389–405.
Cohen, K.M., Gouw, M.J.P., Holten, J.P., 2005. Fluvio-deltaic floodbasin deposits recording differential subsidence within a coastal prism (Central Rhine-Meuse delta, the Netherlands). In: Fluvial Sedimentology VII - IAS Special Publication, 35. Blackwell Scientific, pp. 295–320.
Craig, T.J., Calais, E., Fleitout, L., Bollingerm, L., Scotti, O., 2023. Time-variable strain and stress rated indced by Holocene glacial isostatic adjustment in continental interiors. Tectonophysics 854, 229815. DOI: 10.1016.j.tecto.2023.229815.
Cunningham, A.C., Wallinga, J., 2010. Selection of integration time intervals for quartz OSL decay curves. Quat. Geochronol. 56, 657–666. https://doi.org/10.1016/j.quageo.2010.08.004.
Cunningham, A.C., Wallinga, J., 2012. Realizing the potential of fluvial archives using robust OSL chronologies. Quat. Geochronol. 12, 98–106. https://doi.org/10.1016/j.quageo.2012.05.007.
Damon, A., Mazzotti, S., Vernant, P., Vachon, R., Grosset, J., Ego, F., Baumont, D., 2023. Impact of far-field glacially-induced stresses on fault stability n the eastern Paris Basin. Tectonophysics 864, 230035. https://doi.org/10.1016/j.tecto.2023. 230035.
Demoulin, A., Hallot, E., 2009. Shape and amount of the Quaternary uplift of the western Rhenish shield and the Ardennes (western Europe). Tectonophysics 474, 696–708.
French, H.M., 2017. The Periglacial Environment, Fourth edition. Wiley & Sons Ltd, Hoboken, USA.
Galbraith, R.F., Roberts, R.G., Laslett, G.M., Yoshida, H., Olley, J.M., 1999. Optical Dating of Single and Multiple grains of Quartz from Jinmium Rock Shelter, Northern Australia: part I, Experimental Design and Statistical Models. Archaeometry 41, 339–364. https://doi.org/10.1111/j.1475-4754.1999.tb00987.x.
Gelet, R.M., Marot, D., 2022. Internal erosion by suffusion on cohesionless gap-graded soils: Model and sensibility analysis. Geomech. Energy and the Environ. 31, 100313 https://doi.org/10.1016/j.gete.2022.100313.
Geluk, M.C., Duin, E.J., Dusar, M., Rijkers, R., Van den Berg, M.W., Van Rooijen, P., 1994. Stratigraphy and tectonics of the Roer Valley Graben. Geol. Mijnb. 73, 129–141.
Gold, R.D., Friedrich, A., Kübler, S., Salamon, M., 2017. Apparent late Quaternary fault-slip rate increase in the southern lower Rhine Graben, Central Europe. Bull. Seismol. Soc. Am. 107, 563–580.
Grützner, C., Fischer, P., Reicherter, K., 2016. Holocene surface ruptures of the Rurrand Fault, Germany—insights from palaeoseismology, remote sensing and shallow geophysics. Geophys. J. Int. 204, 1662–1677.
Guerin, G., Mercier, N., Adamiec, G., 2011. Dose-rate conversion factors: update. Ancient TL 29, 5–8.
Hampel, A., Hetzel, R., Maniatis, G., Karow, T., 2009. Three-dimensional numerical modeling of slip rate variations on normal and thrust fault arrays during ice cap growth and melting. J. Geophys. Res. Solid Earth 114, B08406. https://doi.org/10.1029/2008JB006113.
Hicher, P., Marot, D., Sibille, L., 2018. Internal Erosion, 291-334. Advances in Multi-Physics and Multi-Scale Couplings in Geo-Environmental Mechanics. https://doi.org/10.1016/B978-1-78548-278-6.50009-8.
Hiddink, H.A., 2019. Uden-Peelrandbreuk. Archeologisch onderzoek van een laat-middeleeuwse gracht in een profielsleuf aan de Lageburchtweg. Zuidnederlandse Archeologische Notities, 631. VUhbs archeologie, Amsterdam (ISBN 978-90-8614-607-9), p. 44.
Hinzen, K.G., Reamer, S.K., Fleischer, C., 2021. Sesimicity in the Northern Rhine area (1995-2018). J. Seismol. 25, 351–367.
Hoek, W.Z., 2001. Vegetation response to the ~14.7 and ~11.5 ka cal. BP climate transitions: is vegetation lagging climate? Glob. Planet. Chang. 30, 103–115. https://doi.org/10.1016/S0921-8181(01)000.81-9.
Horikoshi, K., Takahashi, A., 2015. Suffusion-induced change in spatial distribution of fine fractions in embankment subjected to seepage flow. Soils Found. 55 (5), 1293–1304. https://doi.org/10.1016/j.sandf.2015.09.027.
Houtgast, G., 1991. Catalogus van Aardbevingen in Nederland. In: Koninlijk Nederlands Meteorologisch Instituut, De Bill, publ, 176, p. 166.
Houtgast, R.F., Van Balen, R.T., 2000. Neotectonics of the Roer Valley rift system, the Netherlands. Glob. Planet. Chang. 27, 131–146.
Houtgast, R.F., Van Balen, R.T., Kasse, C., 2005. Late Quaternary evolution of the Feldbiss Fault (Roer Valley Rift System, the Netherlands) based on trenching, and its potential relation to glacial unloading. Quat. Sci. Rev. 24, 491–510.
Huggett, R., 2016. Fundamentals of Geomorphology, 4th edition. Routledge, London, p. 578.
Huntley, D.J., Baril, M.R., 1997. The K content of the K-feldspars being measured in optical dating or in thermoluminescence dating. Ancient TL 15, 11–13.
Kasse, C., Vandenberghe, D., De Corte, F., Van den Haute, P., 2007. Late Weichselian fluvio-aeolian sands and coversands of the type locality Grubbenvorst (southern Netherlands): sedimentary environments, climate record and age. J. Quat. Sci. 22, 695–708.
Kasse, C., Tebbens, L.A., Trump, M., Deeben, J., Derese, C., De Grave, J., Vandenberghe, D., 2018. Late Glacial and Holocene aeolian deposition and soil formation in relation to the late Paleolithic Ahrensburg occupation, site Geldrop-A2, the Netherlands. Neth. J. Geosci. 71, 3–29.
Kiden, P., Denys, L., Johnston, P., 2002. Late Quaternary Sea-level change and isostatic and tectonic land movements along the Belgian-Dutch North Sea coast: geological data and model results. J. Quat. Sci. 17, 535–546.
Kreemer, C., Blewitt, G., Davis, P.M., 2020. Geodetic evidence for a buoyant mantle plume beneath the Eifel volcanic area, NW Europe. Geophys. J. Int. 222, 1316–1332.
Lapperre, R.E., Kasse, C., Bense, V.F., Woolderink, H.A.G., Van Balen, R.T., 2019. A review of fault zone permeability and associated groundwater level steps in the Roer Valley Rift System. Neth. J. Geosci. https://doi.org/10.1017/njg.2019.4.
Lapperre, R.E., Bense, V.F., Kasse, C., Van Balen, R.T., 2022. Temporal and spatial variability of cross-fault groundwater level differences: the impact of fault-induced permeability reduction, precipitation and evapotranspiration. Hydrogeol. J. https://doi.org/10.1007/s10040-022-02465-w.
McCalpin, J., 2009. Paleoseismology, Second edition. Academic Press London, p. 629.
McDowell-Boyer, L.M., Hunt, J.R., Sitar, N., 1986. Particle Transport through Porous Media. Water Resour. Res. 22, 1901–1921. https://doi.org/10.1029/WR022i013p01901.
Michon, L., Van Balen, R.T., 2005. Characterization and quantification of active faulting in the Roer valley rift system based on high precision digital elevation models. Quat. Sci. Rev. 24, 457–474. https://doi.org/10.1016/j.quascirev.2003.11.009.
Michon, L., Van Balen, R.T., Merle, O., Pagnier, H., 2003. Cenozoic evolution of the Roer Valley Rift System integrated at European scale. Tectonophysics 367, 101–126. https://doi.org/10.1016/S0040-1951(03)00132-X.
Mörner, N.A., 1978. Faulting, fracturing and seismic activity as a function of glacial-isostasy in Fennoscandia. Geology 6, 41–45.
Mörner, N.A., 2013. Patterns in seismology and paleoseismology, and their application on long-term hazard assessments - the Swedish case in view of nuclear waste management. Pattern Recognition in Phys. 1, 75–89.
Müller, B., Zoback, M.L., Fuchs, K., Mastin, L., Gregersen, S., Pavoni, N., Stephanson, O., Ljunngren, C., 1992. Regional patterns of tectonic stress in Europe. J. Geophys. Res. 97, 11783–11803.
Müller, K., Polom, U., Winsemann, J., Stefen, H., Tsukamoto, S., Günther, T., Igel, J., Spies, T., Lege, T., Frechen, M., Franzke, H., Brandes, C., 2020. Structural style and neotectonic activity along the Harz Boundary Fault, northern Germany: a multimethod approach integrating geophysics, outcrop data and numerical simulations. Int. J. Earth Sci. 109 https://doi.org/10.1007/s00531-020-01874-0, 1811e1835.
Murray, A.S., Wintle, A.G., 2003. The single aliquot regenerative dose protocol: potential for improvements in reliability. Radiat. Meas. 37, 377–381. https://doi.org/10.1016/S1350-4487(03)00053-2.
Nowell, D.A.G., Jones, M.C., Pyle, D.M., 2006. Episodic Quaternary volcanism in France and Germany. J. Quat. Sci. 21, 645–675. https://doi.org/10.1002/jqs.1005.
Prescott, J.R., Hutton, J.T., 1994. Cosmic ray contributions to dose rates for luminescence and ESR dating: large depths and long-term time variations. Radiat. Meas. 23, 497–500. https://doi.org/10.1016/1350-4487(94)90086-8.
Reimer, P.J., Bard, E., Bayliss, A., Beck, J.W., Blackwell, P.G., Bronk Ramsey, C., Buck, C.E., Cheng, H., Edwards, R.L., Freidrich, M., Grootes, P.M., Guilderson, T.P., Haflidason, H., Hajdas, I., Hatte, C., Heaton, T.J., Hoffmann, D.G., Hogg, A.G., Hughen, K.A., Kaiser, K.F., Kromer, B., Manning, S.W., Nui, M., Reimer, R.W., Richards, R.A., Scott, E.M., Southon, J.R., Staff, R.A, Turney, C.M.S., Van der Plicht, J., 2013. IntCal13 and Marine13 calibration curves 0-50,000 years BP. Radiocarbon 55, 1869–1887.
Reimer, P.J., Austin, W.E.N., Bard, E., Bayliss, A., Blackwell, P.G., Ramsey, C.B., Butzin, M., Cheng, H., Edwards, R.L., Friedrich, M., Grootes, P.M., Guilderson, T.P., Hajdas, I., Heaton, T.J., Hogg, A.G., Hughen, K.A., Kromer, B., Manning, S.W., Muscheler, R., Palmer, J.G., Pearson, C., van der Plicht, J, Reimer, R.W., Richards, D.A., Scott, E.M., Southon, J.R., Turney, C.S.M., Wacker, L., Adolphi, F., Büntgen, U., Capano, M., Fahrni, S.M., Fogtmann-Schulz, A., Friedrich, R., Kohler, P., Kudsk, S., Miyake, F., Olsen, J., Reinig, F., Sakamoto, M., Sookdeo, A., Talamo, S., 2020. The IntCal20 northern hemisphere radiocarbon age calibration curve (0-55 cal kBP). Radiocarbon 62, 725–757. DOI: 10.1017/ RDC.2020.41.
Sandersen, P.B., Jørgensen, F., 2014. Neotectonic deformation of a late Weichselian outwash plain by deglacation-induced fault reactivation of a deep-seated graben structure. Boreas 44, 413–431.
Schmidt, C., Schaarschmidt, M., Kolb, T., Büchel, G., Richter, D., Zöller, L., 2017. Luminescence dating of late Pleistocene eruptions in the Eifel volcanic field, Germany. J. Quat. Sci. 32, 628–638.
Schokker, J., Koster, E.A., 2004. Sedimentology and facies distribution of Pleistocene cold climate aeolian and fluvial deposits in the Roer Valley Graben (southeastern Netherlands). Permafr. Periglac. Process. 15, 1–20.

Schokker, J., Weerts, H.J.T., Westerhoff, W.E., Berendsen, H.J.A., Den Otter, D., 2007. Introduction of the Boxtel Formation and implications for the Quaternary lithostratigraphy of the Netherlands. Neth. J. Geosci. 86, 197–210.

Smedley, R.K., Duller, G.A.T., Pearce, N.J.G., Roberts, H.M., 2012. Determining the K-content of single-grains of feldspar for luminescence dating. Radiat. Meas. 47, 790–796. https://doi.org/10.1016/j.radmeas.2012.01.014.

Smit, J., Van Wees, J.D., Cloetingh, S., 2018. Early Carboniferous extension in East Avalonia: 350 my record of lithospheric memory. Mar. Pet. Geol. 92, 1010–1027. https://doi.org/10.1016/j.marpetgeo.2018.01.004.

Steffen, R., Wu, P., Steffen, H., Eaton, D.W., 2014. The effect of earth rheology and ice-sheet size on faults slip and magnitude of postglacial earthquakes. Earth Planet. Sci. Lett. 388, 71–80.

Stock, C.S., Smith, E.G.C., 2000. Evidence for different scaling of earthquake source parameters for large earthquakes depending on faulting mechanism. Geophys. J. Int. 143, 157–162.

Thingbaijam, K.K., Martin Mai, P., Goda, K., 2017. New empirical earthquake source-scaling laws. Bull. Seismol. Soc. Am. 107, 2225–2246.

Trippetta, F., Petricca, P., Billi, A., Collettini, C., Cuffaro, M., Lombardi, A.M., Scrocca, D., Ventura, G., Morgante, A., Doglioni, C., 2019. From mapped faults to fault-length magnitudes (FLEM): a test on Italy with methodological implications. Solid Earth 10, 1555–1579. https://doi.org/10.5194/se-10-1555-2019.

Van Balen, R.T., Houtgast, R.F., Van der Wateren, F.M., Vandenberghe, J., Bogaart, P.W., 2000. Sediment budget and tectonic evolution of the Meuse catchment in the Ardennes and the Roer Valley Rift System. Glob. Planet. Chang. 27, 113–130.

Van Balen, R.T., Houtgast, R.F., Cloetingh, S.A.P.L., 2005. Neotectonics of the Netherlands. Quat. Sci. Rev. 24, 439–454.

Van Balen, R.T., Bakker, M.A.J., Kasse, C., Wallinga, J., Woolderink, H., 2019. A late Glacial surface rupturing earthquake at the Peel Boundary fault zone, Roer Valley Rift System, the Netherlands. Quat. Sci. Rev. 218, 254–266.

Van Balen, R.T., Kasse, C., Wallinga, J., Woolderink, H.A.G., 2021. Middle to late Pleistocene faulting history of the Heerlerheide fault, Roer Valley Rift System, influenced by glacio-isostasy and mining-induced displacement. Quat. Sci. Rev. 268, 107111.

Van den Berg, M., Vanneste, K., Dost, B., Lokhorst, A., Van Eijk, M., Verbeeck, K., 2002. Paleoseismic investigations along the Peel Boundary Fault: geological setting, site selection and trenching results. Netherlands. J. Geosci. – Geol. Mijnb. 81, 39–60.

Van der Woude, J., Van Leeuwen, J., 2020. Een gegraven watergang bij de Peelrand als spiegel van de middeleeuwse vegetatie. Grondboor en Hamer 74, 208–213.

Van Eck, T., Davenport, C.A., 1994. Seismotectonics and seismic hazard in the Roer Valley Graben; with emphasis on the Roermond earthquake of April 13, 1992. Geol. Mijnb. 73, 91–92.

Van Hoesel, A., Hoek, W.Z., Braadbaart, F., Van der Plicht, J., Pennock, G.M., Drury, M. R., 2012. Nanodiamonds and wildfire evidence in the Usselo horizon postdate the Allerød-Younger Dryas boundary. Proc. Natl. Acad. Sci. 109, 7648–7653.

Vandenberghe, D., Vanneste, K., Verbeeck, K., Paulissen, E., Buylaert, J.P., De Corte, F., Van den Haute, P., 2009. Late Weichselian and Holocene earthquake events along the Geleen fault in NE Belgium: OSL age constraints. Quat. Int. 199, 56–74.

Vandenberghe, D.A.G., Derese, C., Kasse, C., Van den Haute, P., 2013. Late Weichselian (fluvio-) aeolian sediments and Holocene drift-sands of the classical type locality in Twente (E Netherlands): a high-resolution dating study using optically stimulated luminescence. Quat. Sci. Rev. 68, 96–113.

Vanneste, K., Camelbeeck, T., Verbeeck, K., 2013. A model of composite seismic sources for the lower Rhine Graben, Northwest Europe. Bull. Seismol. Soc. Am. 103, 984–1007.

Vanneste, K., Camelbeeck, T., Verbeeck, K., Demoulin, A., 2018. Morphotectonics and past large earthquakes in eastern Belgium. In: Demoulin, A. (Ed.), Landscapes and Landforms of Belgium and Luxembourg. World Geomorphological Landscapes, pp. 215–236. https://doi.org/10.1007/978-3-319-58239-9_13.

Verbeeck, K., Wouters, L., Vanneste, K., Camelbeeck, T., Vandenberghe, D., Beerten, K., Rogiers, B., Schiltz, M., Burow, C., Mees, F., De Grave, J., Vandenberghe, N., 2017. Episodic activity of a dormant fault in tectonically stable Europe: the Rauw fault (NE Belgium). Tectonophysics 699, 146–163.

Wallinga, J., Murray, A., Wintle, A., 2000. The single-aliquot regenerative-dose (SAR) protocol applied to coarse-grain feldspar. Radiat. Meas. 32, 529–533. https://doi.org/10.1016/S1350-4487(00)00091-3.

Wallinga, J., Sevink, J., Van Mourik, J.M., Reimann, T., 2019. Chapter 4 - Luminescence dating of soil archives. In: Van Mourik, J.M., Van Der Meer, J.J.M. (Eds.), Developments in Quaternary Sciences, vol. 18. Elsevier, pp. 115–162. https://doi.org/10.1016/B978-0-444-64108-3.00004-5.

Wells, D.L., Coppersmith, K.J., 1994. New empirical relationships among magnitude, rupture length, rupture width, rupture area, and surface displacement. Bull. Seismol. Soc. Am. 84, 974–1002.

Wesnousky, S.G., 2006. Predicting the endpoints of earthquake ruptures. Nature 444, 358–360. https://doi.org/10.1038/nature05275.

Woolderink, H.A.G., Kasse, C., Cohen, K.M., Hoek, W.Z., Van Balen, R.T., 2018. Spatial and temporal variations in river terrace formation, preservation, and morphology in the lower Meuse Valley, the Netherlands. Quat. Res. 91, 548–569. https://doi.org/10.1017/qua.2018.49.

Woolderink, H.A.G., Kasse, C., Grooteman, L.P.A., Van Balen, R.T., 2019. Interplay between climatic, tectonic and anthropogenic forcing in the lower Rhine Graben, the Roer River. Geomorphology 344, 25–45.

Worum, G., Van Wees, J.D., Bada, G., Van Balen, R.T., Cloetingh, S.A.P.L., 2004. Slip tendency analysis as a tool to constrain fault reactivation: a numerical approach applied to 3D fault models in the Roer Valley Rift System (SE Netherlands). J. Geophys. Res. 109, B02401. https://doi.org/10.1029/2003JB002586.

Worum, G., Michon, L., Van Wees, J.D., Van Balen, R.T., Cloetingh, S., Pagnier, H., 2005. Pre-Neogene controls on present-day fault activity in the West Netherlands Basin and Roer Valley Rift System (southern Netherlands): role of variations in fault orientation in a uniform low-stress regime. Quat. Sci. Rev. 24, 475–490.

Zhong, N., Li, H., Jiang, H., Lu, H., Zheng, Y., Han, S., Ye, J., 2020. Typical Soft-Sediment Deformation Structures Induced by freeze/Thaw Cycles: a Case Study of Quaternary Alluvial Deposits in the Northern Qiangtang Basin. Tibetan Plateau. Acta Geol. Sin. (English Edition) 94 (1), 176–188. https://doi.org/10.1111/1755-6724.14345.

Ziegler, P.A., 1992. European Cenozoic rift system. Tectonophysics 208, 91–111.